Geophysical Journal International

*Geophys. J. Int.* (2024) **236,** 1089–1105
Advance Access publication 2023 December 06
GJI Seismology

https://doi.org/10.1093/gji/ggad470

# New constraints on the shear wave velocity structure of the Ivrea geophysical body from seismic ambient noise tomography (Ivrea-Verbano Zone, Alps)

M. Scarponi,[1,*] J. Kvapil,[1] J. Plomerová,[1] S. Solarino[2] and G. Hetényi[3]

[1]*Institute of Geophysics, Czech Academy of Sciences, Prague,* 14100*, Czech Republic. E-mail: matteo.scarponi@univ-lyon1.fr*
[2]*Istituto Nazionale di Geofisica e Vulcanologia INGV, DICCA Università di Genova, Genoa,* 16145*, Italy*
[3]*Institute of Earth Sciences, University of Lausanne, Lausanne,* 1015*, Switzerland*

Accepted 2023 December 5. Received 2023 October 26; in original form 2023 July 7

## SUMMARY

We performed seismic ambient noise tomography to investigate the shallow crustal structure around the Ivrea geophysical body (IGB) in the Ivrea-Verbano Zone (IVZ). We achieved higher resolution with respect to previous tomographic works covering the Western Alps, by processing seismic data collected by both permanent and temporary seismic networks (61 broad-band seismic stations in total). This included IvreaArray, a temporary, passive seismic experiment designed to investigate the IVZ crustal structure. Starting from continuous seismic ambient noise recordings, we measured and inverted the dispersion of the group velocity of surface Rayleigh waves (fundamental mode) in the period range 4–25 s. We obtained a new, 3-D $v_S$ model of the IVZ crust via the stochastic neighbourhood algorithm (NA), with the highest resolution between 3 to 40 km depth. The fast and shallow shear wave velocity anomaly associated with the IGB presents velocities of 3.6 km s$^{-1}$ directly at the surface, in remarkable agreement with the location of the exposed lower-to-middle crustal and mantle outcrops. This suggests a continuity between the surface geological observations and the subsurface geophysical anomalies. The fast IGB structure reaches $v_S$ of 4 km s$^{-1}$ at 20–25 km depth, at the boundary between the European and Adriatic tectonic plates, and in correspondence with the earlier identified Moho jump in the same area. The interpretation of a very shallow reaching IGB is further supported by the comparison of our new results with recent geophysical investigations, based on receiver functions and gravity anomaly data. By combining the new geophysical constraints and the geological observations at the surface, we provide a new structural interpretation of the IGB, which features lower crustal and mantle rocks at upper crustal depths. The comparison of the obtained $v_S$ values with the physical properties from laboratory analysis of local rock samples suggests that the bulk of the IGB consists of a combination of mantle peridotite, ultramafic and lower crustal rocks, bound in a heterogeneous structure. These new findings, based on $v_S$ tomography, corroborate the recent interpretation for which the Balmuccia peridotite outcrops are continuously linked to the IGB structure beneath. The new outcomes contribute to a multidisciplinary framework for the interpretation of the forthcoming results of the scientific drilling project DIVE.

DIVE aims at probing the lower continental crust and its transition to the mantle, with two ongoing and one future boreholes (down to 4 km depth) in the IVZ area, providing new, complementary information on rock structure and composition across scales. In this framework, we constrain the upper crustal IGB geometries and lithology based on new evidence for $v_S$, connecting prior crustal knowledge to recent active seismic investigations.

**Key words:** Continental crust; Seismic noise; Seismic tomography; Continental tectonics: compressional; Crustal structure.

*Now at: Laboratoire de Géologie de Lyon, Terre, Planètes, Environnement, Université Lyon 1, Villeurbanne, France.

## 1 INTRODUCTION

The Ivrea-Verbano Zone (IVZ) is located along the inner arc of the Western Alps (Europe) and represents a long-recognized, open-air geological and geophysical laboratory for the study of both the Earth's crust and mantle. Bounded to the north by the Insubric segment of the Periadriatic Line (PL, Schmid *et al.* 1989), the IVZ lies at the frontier between the European and the Adriatic tectonic plates (Schmid *et al.* 2004; Petri *et al.* 2019), which were involved in the Alpine continental collision that began at *ca*. 35 Ma (Handy *et al.* 2010, 2015).

The IVZ exposes lower-to-middle crustal composition rocks outcropping at the surface, and is regarded as an almost-unique and nearly complete cross-section of the continental crust (Fig. 1, Fountain 1976; Zingg *et al.* 1990; Khazanehdari *et al.* 2000). It also exposes mantle peridotite rocks; among these, the Balmuccia peridotite is the largest outcropping mantle unit at the surface (Fig. 1), bounded by a mafic lower crustal complex (e.g. Rivalenti *et al.* 1975, 1981; Quick *et al.* 1995, 2003).

In this study, we focus on the high-density high seismic-velocity anomaly beneath the IVZ surface, which extends up to shallow depths (i.e. below 10 km depth) known as the Ivrea geophysical body (IGB, e.g. Kissling *et al.* 1984). We aim to image and model the IGB structure and surroundings in terms of absolute shear wave velocity ($v_S$). The IGB constitutes the root of the IVZ and it is closely related (if not directly linked) to the exposed geological units at the surface. It is characterized by an anomalously dense and seismically fast structure (e.g. Berckhemer 1968; Bürki 1990; Solarino *et al.* 2018; Scarponi *et al.* 2020, 2021), which extends along the whole inner arc of the Western Alps in correspondence with the European–Adriatic continental collision boundary. This anomaly features along-strike variations, especially in the depth of its uppermost structure, and potentially outcrops at the surface in the IVZ. Interpreted as a sliver of Adriatic lower lithosphere (e.g. Schmid *et al.* 2017), and emplaced at shallow depth during the European–Adriatic tectonic collision, the IGB has been the subject of multiple geophysical investigations since the early work of Niggli (1947).

The IGB was first imaged via active refraction and reflection seismic experiments (e.g. Closs & Labrouste 1963; Berckhemer 1968; Ansorge 1979; Thouvenot *et al.* 1990), which provided new geophysical evidences for geodynamic and tectonic interpretation of the Alps (e.g. Schmid & Kissling 2000) and structural constraints for the development of IGB density models via gravity anomaly analysis (e.g. Berckhemer 1968; Kissling *et al.* 1984; Bayer *et al.* 1989; Bürki 1990). These studies both exploited and showed the technical limitations of active seismic experiments, especially in imaging the strongly and laterally varying crustal structure associated with the IGB (Kissling 1993), beneath a terrain that is challenging to instrument in an optimal manner (topographic map in Fig. S0, Supporting Information).

The increasing seismic data availability in the Alps (e.g. Hetényi *et al.* 2018) and the advent of modern seismic tomographic techniques allowed to image the western Alps and the IGB at regional scales with improving resolution, by exploiting both local (e.g. Paul *et al.* 2001; Diehl *et al.* 2009; Solarino *et al.* 2018) and teleseismic earthquake events (e.g. Lippitsch *et al.* 2003; Kissling *et al.* 2006), traveltime analysis (e.g. De Franco *et al.* 1997) and seismic ambient noise recordings (e.g. Kästle *et al.* 2018; Lu *et al.* 2018; Zhao *et al.* 2020; Nouibat *et al.* 2022). Seismic receiver functions (RF) were also employed to map the IGB geometry and its physical properties at key locations along the European–Adriatic collision boundary (e.g. Zhao *et al.* 2015; Salimbeni *et al.* 2020; Colavitti *et al.* 2022; Paul *et al.* 2022).

Nevertheless, the data sets in these works did not have sufficient resolution for a detailed investigation of the local IGB structure and physical properties beneath the IVZ geological units, nor to address key open questions such as: what is the connection between the shallow IGB anomaly and the outcropping rocks of lower-to-middle crustal composition in the IVZ? How do the structure and the composition of the IGB vary with depth?

Establishing whether a continuous link between IVZ surface geological units and shallow geophysical anomalies exists or not is key to better understand the IVZ's tectonic emplacement, investigate the existence and the status of a former Moho and, more generally, to study how crustal-scale deformation occurs in continental collision zones.

Multiple studies have taken steps towards these questions recently, as forerunners of the scientific drilling project DIVE (www.dive2ivrea.org, Pistone *et al.* 2017). Benefitting from new seismic and gravity data (Hetényi *et al.* 2017; Scarponi *et al.* 2020), recent multidisciplinary geophysical investigations provided new constraints on the IGB 3-D density distribution, geometry and composition at intracrustal to kilometric scales beneath in the IVZ. These have clearly delineated the contours of a denser and seismically faster structure, reaching as shallow as $1 \pm 1$ km depth below sea level (Scarponi *et al.* 2020, 2021), with physical properties in agreement with ultramafic mantle rock types. Pistone *et al.* (2020) investigated the composition of the IGB at depth by comparing petrophysical modelling with density (Scarponi *et al.* 2020) and larger scale $v_P$ constraints (Diehl *et al.* 2009), pointing at a predominantly lower crustal body for the IGB. However, no constraints on $v_S$ were available for the same analysis (Pistone *et al.* 2020).

Recent high-resolution, shallow $v_P$ tomography from active source seismics suggests that the IVZ Balmuccia peridotite represents the tip of a wider, buried mantle body, which is continuously linked to the IGB at depth (Ryberg *et al.* 2023). This recent finding favours the idea of a fossil crustal–mantle transition zone being close to and at the surface (e.g. Rivalenti *et al.* 1975; Zingg *et al.* 1990), against the interpretation of isolated peridotite lenses in Balmuccia (e.g. Quick *et al.* 2003). However, Ryberg *et al.* (2023) provide local $v_P$ constraints down to only *ca*. 3 km depth below the surface. To follow up on investigating the structural link by imaging bulk seismic properties in 3-D, and to constrain the IGB composition as well, within the same framework of the most recent passive geophysical investigations (e.g. Scarponi *et al.* 2020, 2021), we performed seismic ambient noise tomography (ANT) in the area.

The ANT analysis provides new, 3-D high-resolution geophysical constraints on absolute $v_S$ beneath the IVZ at intracrustal scales, with the highest resolution between *ca*. 3 km and a maximum depth of 40 km.

## 2 DATA

We collected continuous broad-band seismic data, organized in daily files, from the permanent seismic networks of Switzerland and Italy (FDSN network codes IV, GU, MN, CH; Fig. 1—see Data Availability statement for full data reference). To improve the data coverage and the resolution with respect to the previous tomographic studies constraining $v_S$ across the Western Alps, we also processed the seis-

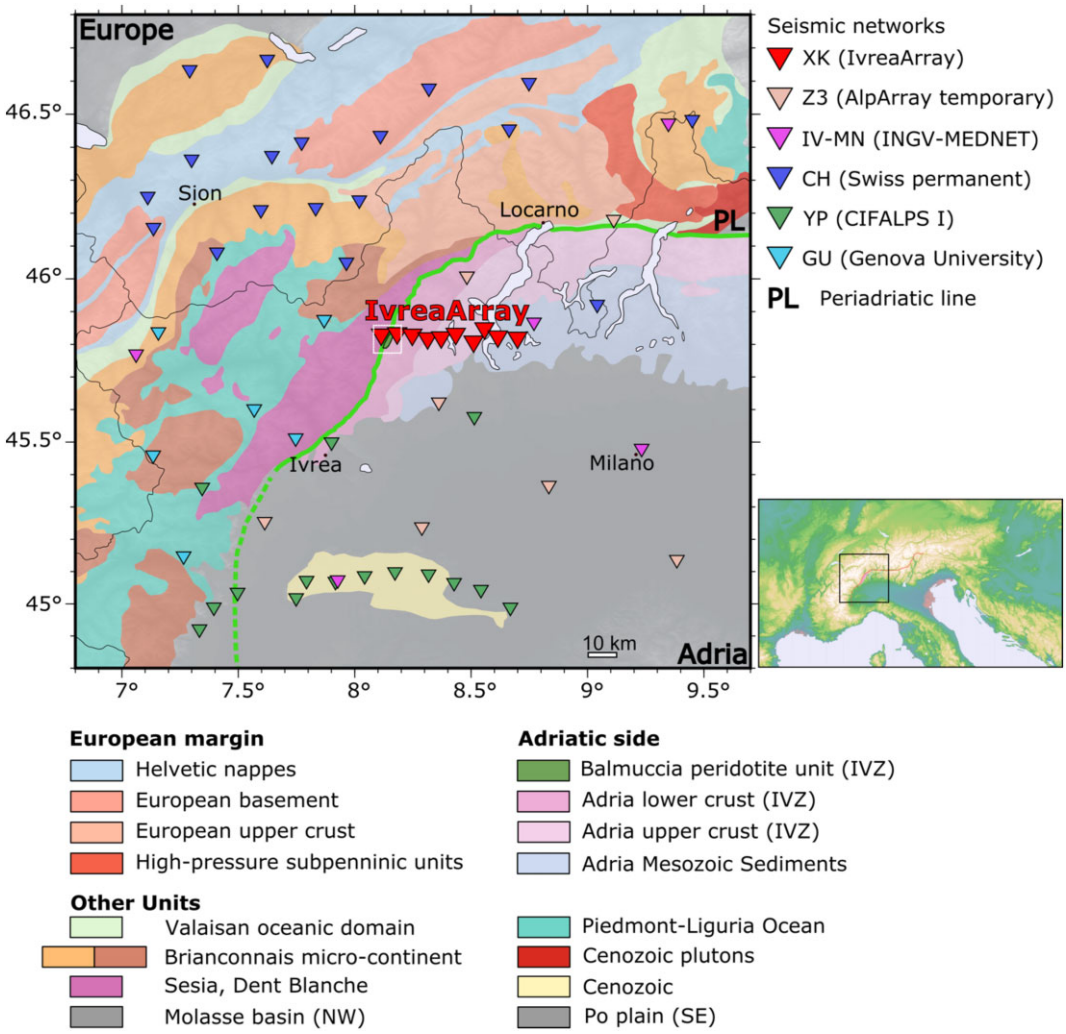


**Figure 1.** Tectonic map of the IVZ and surrounding region in the Western Alps, with simplified tectonic units after Schmid *et al.* (2004). The PL in green separates the main European and Adriatic tectonic domains at the surface. The seismic stations used for this study are shown as triangles, coloured according to the respective operating network (see the legend). The white dashed rectangle to the western portion of IvreaArray indicates the location of the Balmuccia mantle peridotite outcrop.

mic data collected from the passive seismic experiment CIFALPS I (Zhao *et al.* 2016, network code YP), and the temporary seismic stations operated in the frame of the cooperative AlpArray project (Hetényi *et al.* 2018, network code Z3). These data sets were merged with the seismic recordings of the IvreaArray passive experiment (Hetényi *et al.* 2017; Scarponi *et al.* 2021, Fig. 1), which was established to better image the IGB in the IVZ. IvreaArray operated 10 broad-band seismic stations from the MOBNET pool of the IGCAS (Institute of Geophysics of the Czech Academy of Sciences, https://www.ig.cas.cz/en/) from 2017 June to 2019 September, which crossed the IVZ along a west–east linear profile at 5 km interstation spacing. Overall, we processed seismic data from 61 broad-band seismic stations (Fig. S1 Supporting Information, for data availability plot versus time), centred on the IVZ and IvreaArray, providing a good ray path and azimuthal coverage (Fig. S2 Supporting Information).

The collected ambient noise data set was then partially reduced to account for one of the fundamental assumptions of seismic ANT: the isotropic distribution of noise sources (Lobkis & Weaver 2001). In fact, the isotropic distribution of noise sources is usually not satisfied within continental Europe during winter. Numerous studies have shown that seismic noise in continental Europe is dominated by the surface waves generated in the Atlantic Ocean (e.g. Stehly *et al.* 2006; Yang & Ritzwoller 2008; Lu *et al.* 2018, among others), which significantly affects the spatial distribution of the noise sources in the period band of interest here (4–25 s). The analysis of the European seismic noise field suggests that seismic noise below 20 s period can be considered as isotropic during summer, rather than winter time (e.g. Yang & Ritzwoller 2008; Kvapil *et al.* 2021), which was also observed on a test subset of our database. Therefore, following the approach of, for example, Kvapil *et al.* (2021) and Pedersen *et al.* (2023), we restricted our data selection to the summer months of June, July and August. We ultimately obtained ambient noise data for 1830 station pairs. Most of the stations provided simultaneous recordings for up to three sets of summer data (2017–2019 June–August) except for CIFALPS I stations, which operated for *ca*. 14 months until 2013 September (Zhao *et al.* 2016). Permanent stations provided summertime data both for the year 2013, and from the year 2017 to 2019, which coincides with the time span of the CIFALPS I and the IvreaArray temporary passive seismic experiments respectively. Interstation distances range from 5 to 240 km.

## 3 METHOD

We invert surface wave velocity dispersion curves, derived from ambient noise data recorded simultaneously at various seismic stations, to obtain the distribution of $v_S$ in the subsurface. This class of methods has proven to be effective from local (e.g. Lehujeur *et al.* 2018; Schippkus *et al.* 2020; Qorbani *et al.* 2022) to regional (e.g. Molinari *et al.* 2015b; Kästle *et al.* 2018; Kvapil *et al.* 2021) and global scales (Nishida *et al.* 2009; Schimmel *et al.* 2011). In general, the propagation of surface seismic waves is dispersive: as a function of their period, they sample different depth ranges in the crust and uppermost mantle, and thus they are sensitive to the respective velocities at depth. By quantifying this dispersion across a range of periods, the variation of $v_S$ in the subsurface can be reconstructed. In the ANT framework, we measure the surface wave dispersion properties without relying on any signal from earthquake sources (e.g. Levshin & Ritzwoller 2001; Lobkis & Weaver 2001; Shapiro & Campillo 2004).

We processed the vertical component of the recorded ground motion to measure and invert the dispersion curves of the fundamental mode of Rayleigh waves (group velocities) in order to obtain a 3-D isotropic $v_S$ model of the crust. Inverting phase velocity dispersion curves can provide useful complementary information as well. However, most methods for measuring phase velocity dispersion curves provide non-unique solutions (e.g. Ekström et al. 2009, among others). This non-uniqueness is usually addressed by considering realistic reference velocity values for $v_S$ or a known relationship between phase and group velocities. However, the complex and heterogeneous study area (IVZ, Fig. 1) features lower-to-middle crustal rocks at shallow depths, next to upper crustal units and major sedimentary basins (e.g. Po plain—Molinari *et al.* 2015a). The choice of reference values for $v_S$ would be subjective and prone to user interpretation error. Hence, we chose to analyse group velocities in this framework. The addition of phase velocity inversion, as well as Love waves inversion, will be proposed in subsequent studies.

The taken steps include: preliminary data processing; station-pair cross-correlation (CC) and stacking; frequency–time dispersion analysis (FTAN); periodwise computation of 2-D surface group-velocity maps and inversion of the 2-D maps for local 1-D velocity profiles, which, juxtaposed together, form the final 3-D model across the study area. These steps are presented below.

Following Bensen *et al.* (2007), we homogeneously pre-processed the raw data to enhance the ambient noise against other types of signal. We remove instrument response, bandpass-filtered the data in the 0.2–100 s period range (i.e. 0.01–5 Hz) and resampled the traces at 10 samples per second. To minimize the effect of coherent signals from local earthquake events without losing dispersion information, we performed amplitude normalization: each data point has been normalized by the mean amplitude of the selected moving window (Bensen *et al.* 2007).

The pre-processed data set was used to compute CC traces for each station pair. We used the MSNoise software package, from Lecocq *et al.* (2014), to store the seismic ambient noise data based on network, station, simultaneous recording time, to perform spectral whitening and to compute station-pairwise CC traces accordingly. For the CC task, we have split all the pre-processed waveforms in 1-hr segments with 50 per cent overlap and used a maximum CC lag time of 480 s. This maximum lag time, together with a maximum interstation distance of 200 km, ensured that we could measure low surface wave velocities (down to 1 km s$^{-1}$), which are expected for sediments in the Po plain in the south-eastern part of our study area (Molinari *et al.* 2015a). Finally, the cross-correlated hourly traces were stacked to obtain one CC trace for each station pair (see Fig. S3 Supporting Information, for CC examples as a function of station-pair distance and for different period ranges of interest).

We applied FTAN (Levshin & Ritzwoller 2001) to measure the dispersion of the Rayleigh wave fundamental mode group velocities. This analysis provides average dispersion information along each station-pair path. To perform this, we used the empirical approximations of the group Green's functions (EGFs), computed from the processed ambient noise data; the EGFs were obtained by taking the average of the causal and acausal sides of each CC trace, and by computing the time derivative (with reversed sign) of the associated envelope (Lin *et al.* 2008). We still observed some amount of asymmetry in the causal and acausal portions of the EGFs, in the 5 to $<$ 20 s period range. A similar asymmetry was also observed across other EGFs from ambient noise data collected in Europe (e.g. Yang & Ritzwoller 2008; Lu *et al.* 2018, among others). We argue that this is due to the directionality of the noise sources, which we addressed as much as possible by performing our analysis in the summer season.

In the FTAN, we filtered the obtained EGFs in narrow-frequency bands in the period range from 25 s down to 2 s, using a scaling factor of 1.4 to define each frequency band with respect to its central frequency $f_0$ (i.e. $[\frac{f_0}{1.4}, f_0 * 1.4]$), and measured the group velocities for each period and station pair. We automated the measurement of group-velocity dispersion curves starting from a minimum period of 2 s where available. The maximum period of investigation was determined by the associated wavelength, which was required not to be longer than half the interstation distance, for each station pair (following e.g. Lin *et al.* 2008; Boschi *et al.* 2013, among others). Moving from longer to shorter periods, the automated picking process stopped either when the signal became too weak, that is, signal-to-noise ratio (SNR) lower than 5, or when picking became ambiguous because of several branches and local peaks in the diagram (Figs 2a–c). We manually re-inspected all the picks and finally stored dispersion curves for 1186 station pairs.

The measurement example for three station pairs in in Fig. 2 shows that including the IvreaArray seismic stations did provide higher resolution constraints across the study area—in particular, when mapping the transition from the slower Po plain area to the faster crustal structures in the IVZ (Figs 2b and c), and when mapping the transition from the IVZ to the northwest across the collision boundary (Figs 2a and c).

Next, we computed 2-D surface group-velocity maps in the 4–25 s period range (most complete range of measurements across the study area), using the Fast Marching Surface Tomography package (FMST, Rawlinson 2005). FMST solves an inverse problem to map the measured station-pair group velocities onto a regular grid, producing 2-D surface group-velocity maps. Based on our seismic station distribution, we set the horizontal grid spacing at 10 km by 10 km across the study area (e.g. Fig. 3, see Fig. S4 Supporting Information, for 2-D maps at selected periods). For each period, we performed a seven-iteration inversion starting from a constant 2-D velocity field of 2.5 km s$^{-1}$. Assembling the obtained 2-D maps provided local Rayleigh dispersion information, allowing extraction of local dispersion curves, one for each point of the final model grid (Fig. 3). Following the approach of previous authors (e.g. Mordret *et al.* 2015; Sánchez-Pastor *et al.* 2021), we estimated the effect of topography on our ambient noise dispersion measurements. We evaluated the change in interstation distances,

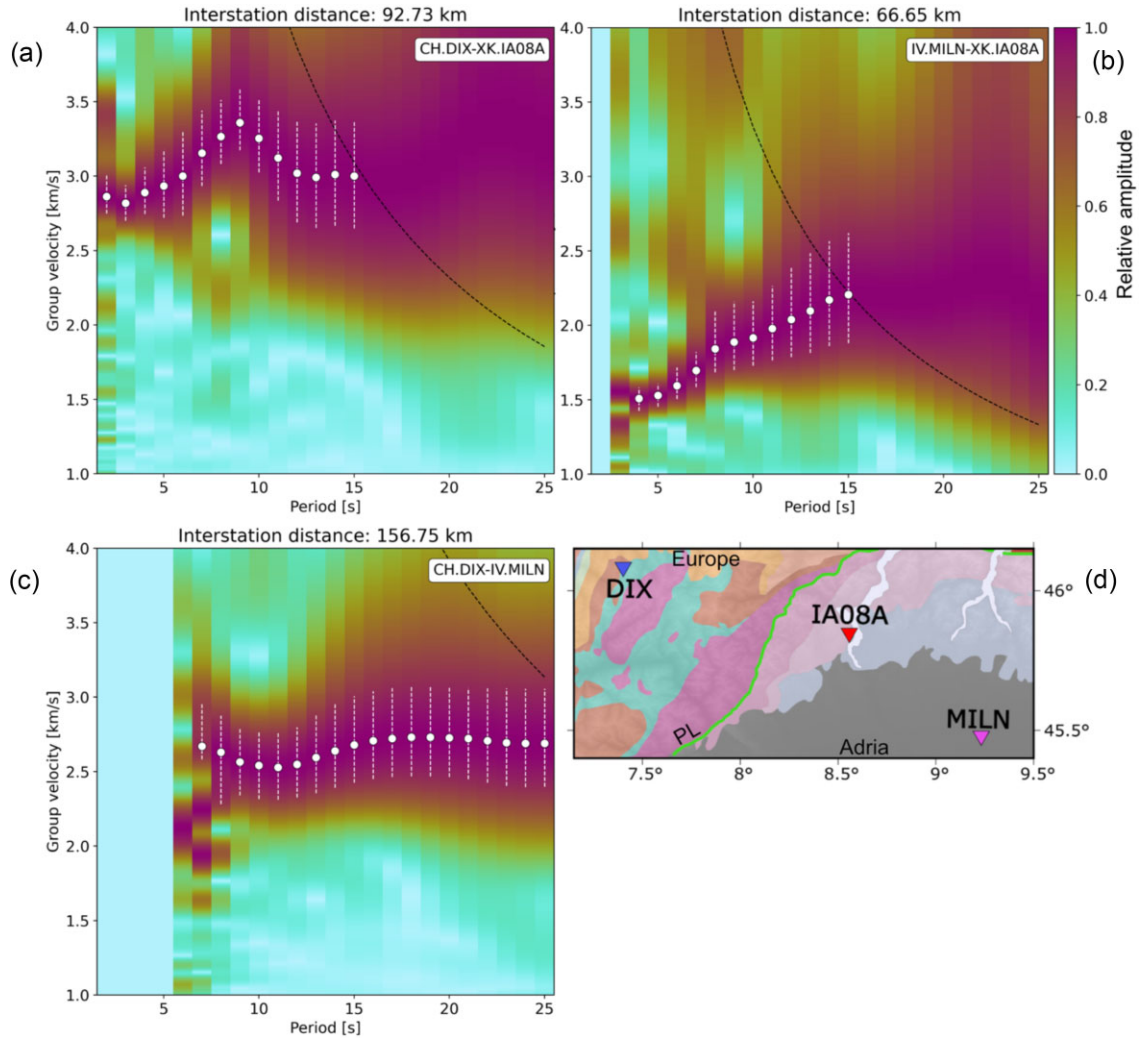


**Figure 2.** FTAN (Levshin & Ritzwoller 2001) used to measure the dispersion curves of Rayleigh waves group velocity from seismic ambient noise. The two-station analysis is here shown for three pairs of stations (see locations in d): (a) DIX and IA08A (dispersion curve with a local maximum at 10 s), (b) IA08A and MILN (monotonously increasing dispersion curve) and (c) DIX and MILN (dispersion curve with a local minimum at 10 s). The white dots indicate the measured group velocities at each period and the thin vertical bars indicate the group envelope width at 80 per cent of its maximum for uncertainty estimation (see Section 4). The thin black curve indicates the region in which the group-velocity assessment is not performed due to too short interstation distances.

with and without station elevation differences, for IvreaArray stations. In particular, IvreaArray presents the smallest interstation distances within our database, spanning from 777 to 250 m altitude, at the transition between Po plain and the pre-alpine area. As interstation distance variation is less than 1 per cent, we regard its effect as negligible for our application. As a final step, we inverted the local dispersion curves for 1-D $v_S$ profiles by means of the stochastic neighbourhood algorithm (NA) via Dinver software (Wathelet 2008). We parametrized the 1-D $v_S$profiles as six horizontal, variable-thickness layers over a half-space, with each layer being associated with a velocity gradient implemented by five sublayers of constant velocity. We did not impose any further constraints on the velocity variation across the layer interfaces, allowing also discontinuous velocity changes with depth, as they could not be excluded *a priori* (see Fig. S5 Supporting Information, for inversion tests with increasingly tighter constraints on $v_S$, along the IvreaArray profile). We chose six layers to possibly account for shallow sediments, upper, middle and lower crustal structures, and eventually two uppermost mantle layers above the homogeneous half-space.

The Moho map from Spada *et al.* (2013) documents a significant jump across the Europe–Adria tectonic boundary, though partially unresolved, and presents spatially smooth interfaces elsewhere in the study area. Hence, we decided to invert the data without additional a priori constraints and we assigned an initial Moho depth of 30 km, allowing up to 20 per cent depth variation for each interface during the inversion. We used the Moho map from Spada *et al.* (2013) for later comparison with our results. Eventually, we performed a test inversion *a priori* including the available Moho model of Spada *et al.* (2013), obtaining consistent results with the final ones.

We point out that NA performs a statistical search across the model space (i.e. the ensemble of all the candidate crustal models for our problem), and provides the solution as an ensemble of statistically relevant models (Sambridge 1999; Sambridge & Mosegaard 2002). Consequently, we do not provide a single starting model for the inversion, but rather the allowed value ranges for all of the model parameters, shown in Table 1.

In particular, the NA stochastic exploration of the model space is guided based on two inversion parameters: number of initial models ($n_0$) and number of newly generated models at each iteration ($n_r$). For

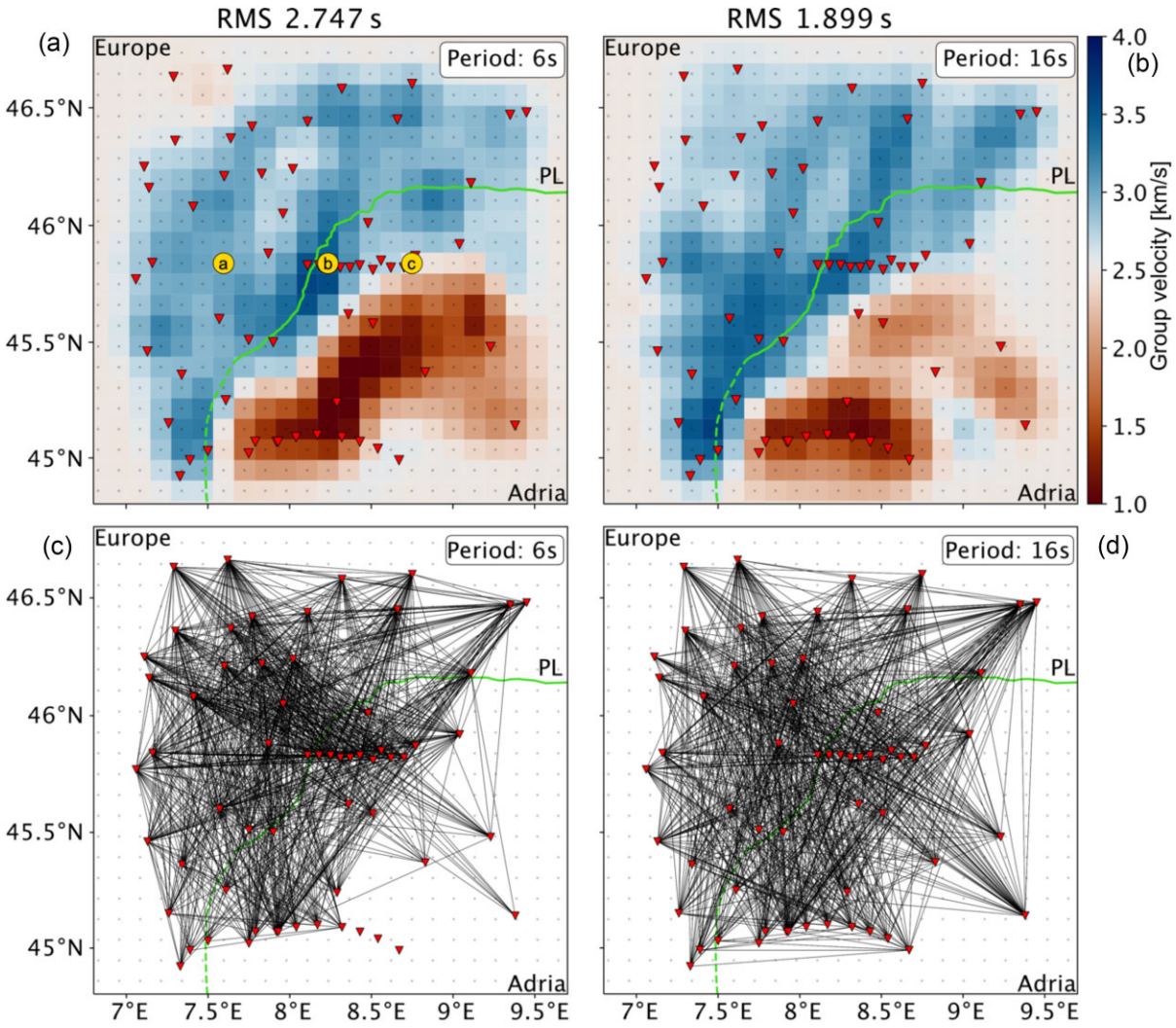


**Figure 3.** (a) and (b) Examples of 2-D group-velocity maps from the FMST method (Rawlinson 2005) selected at 6 and 16 s periods, chosen from the 4 to 25 s range analysed in this work. The three yellow circles in panel (a) show the locations of the 1-D profiles in Fig. 4. (c) and (d) Ray coverage for the dispersion measurements obtained at 6 and 16 s. The PL in green and the seismic stations as red triangles are shown for reference. Grey dots indicate the 10 km by 10 km gridpoints where the 2-D velocity maps were retrieved.

**Table 1.** Summary of the parameters and their ranges used in the stochastic NA inversion (Wathelet 2008), to obtain 1-D $v_S$ velocity profiles from local group dispersion measurements.

| Layer | $v_S$ (km s$^{-1}$) | Bottom depth (km) | $v_P$ (km s$^{-1}$) | Density (kg m$^{-3}$) | Poisson's ratio | Number of sublayers | Structure change |
|---|---|---|---|---|---|---|---|
| Near surface | 1.2–4.3 | 0.1–9 | 3.3–5.5 | 2.0–3.5 | 0.2–0.5 | 5 | Positive linear gradient |
| Upper crust | 2.5–4.3 | 12–18 | 5.0–7.0 | 2.7–3.5 | 0.2–0.5 | 5 | Linear gradient |
| Middle crust | 3.0–4.3 | 18–27 | 5.0–7.0 | 2.7–3.5 | 0.2–0.5 | 5 | Linear gradient |
| Lower crust | 3.0–4.3 | 24–36 | 6.5–8.0 | 2.9–3.5 | 0.2–0.5 | 5 | Linear gradient |
| Uppermost mantle 1 | 3.0–4.5 | 47–53 | 7.0–8.5 | 3.1–3.5 | 0.2–0.5 | 5 | Linear gradient |
| Uppermost mantle 2 | 3.0–4.9 | 70 | 7.0–9.0 | 3.1–3.5 | 0.2–0.5 | 5 | Linear gradient |
| Half space | 3.0–5.0 | – | 7.0–9.0 | 3.1–3.5 | 0.2–0.5 | – | None (homogeneous) |

each inversion, we used 500 starting models, and 200 new models generated for each of 300 iterations; in total, we tested 60 500 1-D $v_S$ models at each gridpoint. Finally, we defined the local 1-D velocity profiles as the average of the 10 per cent (i.e. 6050) best-performing models.

## 4 UNCERTAINTY, RESOLUTION AND SENSITIVITY

We discuss the main sources of uncertainty and how they were identified and treated within our multistep inversion process. For

the sake of the uncertainty estimation of traveltime measurements from EGFs, and for consistency with respect to the FTAN analysis and the FMST software, in this section we discuss *group traveltime* measured between two stations instead of *group velocity*: for a given period and a given station pair, the measured *group velocity* equals the interstation distance over measured *traveltime* (i.e. $v_{meas} = d/t_{meas}$). The traveltime uncertainties were then used as input in the FMST package, for the computation of 2-D surface group-velocity maps.

For this reason, we designed a procedure to evaluate the uncertainties on traveltime measurements, based on the EGFs peak width's distribution across all the station pairs. In particular, we measured the group envelope widths at 80 per cent of the envelope's maximum amplitude for each period of interest: the wider the peak with respect to the period mean, the higher the uncertainty (see the white dashed segments in Figs 2a–c, e.g. of peak width measurements, and Fig. S6, Supporting Information, for peak width distributions at selected periods). First, we attributed a minimum uncertainty of 0.1 s to the traveltime measurements. Then, we linearly increased the uncertainty to 0.5 s, for those arrivals whose width was between 1 and 2 standard deviations (STD) higher than the mean. Finally, we linearly increased the uncertainty from 0.5 to 2 s for those, whose width was between 2 and 3 STDs higher than the mean; and kept 2 s beyond. Within FMST, 0.5 s uncertainty resulted in a smaller input weight and 2 s uncertainty makes the traveltime datum negligible for the sake of the 2-D inversion. We compared our uncertainty estimates to those obtained by recomputing the EGFs with random subsets of daily CC traces (*ca*. 30 per cent of the database for one test station pair), and obtained consistent results. We consider that our procedure provides a rather conservative uncertainty estimate.

Subsequently, we performed resolution tests for the computation of the 2-D surface velocity maps, to estimate the spatial scales and velocity anomalies we could constrain given our data coverage. We inverted synthetic traveltimes, generated for a random 2-D surface velocity distribution (following e.g. Verbeke *et al.* 2012; Molinari *et al.* 2015b), ranging from 1.5 to 4 km s$^{-1}$. Prior to the synthetic test, we added random Gaussian noise (with 0.1 s mean and 0.1 s STD) to the synthetic observations (see Fig. S7 Supporting Information, for resolution tests at selected periods).

We also performed extensive testing to find a combination of smoothing and damping parameters which (1) did not provide any single cell velocity perturbations; (2) did not provide velocity perturbations beyond the 1–4 km s$^{-1}$ boundaries and (3) did not provide velocity patterns correlated with the ray path distribution at any period (see Fig. S8 Supporting Information, for an example of root-mean-square RMS error, model variance and model roughness variation as a function of smoothing and damping parameter values). Finally, we identified 20 km (i.e. two grid cells size) as the minimum length-scale we could resolve, in particular at upper crustal depths where the resolution at the shortest periods we employed is the highest (Figs 4g–i).

Concerning the NA inversion, the sensitivity kernels computed for the final 1-D $v_S$ velocity models for our period range of interest (4–25 s), show a decrease in sensitivity for $v_S$ at *ca*. 30–35 km depth (Figs 4g–i). While the sensitivity does not decay to zero (Figs 4g–i), the upper and middle crustal depths remain the best resolved areas for the period range used in this work. Typical lower crustal depths represent the lower limit of our depth resolution. While we observe a Moho-related velocity increase, which is smoother on the European side than the Adriatic counterpart (Figs 4d–f), this suggests not to interpret additional velocity features below the Moho discontinuity across our study area.

Eventually, we infer the Moho-related velocity gradient at 30–50 km depths depending on the location.

Concerning the final 1-D $v_S$ profiles obtained from the NA inversion, we obtained a maximum 0.15 km s$^{-1}$ STD of $v_S$ values within the best 10 per cent performing models, and we regard this as a suitable estimate for the uncertainty on the final $v_S$ velocity values.

## 5 RESULTS

We built the final 3-D $v_S$ model underlying the IVZ by juxtaposing the local 1-D velocity profiles, which were obtained in the NA inversion at each model gridpoint. We applied nearest point interpolation and a Gaussian filter with a 5 km length-scale to produce vertical cross-sections of the model. The 3-D model provides a satisfactory fit of the dispersion data across the sampled volume (e.g. Figs 4a–c) and presents first-order variations in the velocity structure across the different tectonic domains in our study area.

We can pinpoint these structural differences by looking at the different $v_S$ profiles reported in Figs 4(d)–(f). Each of them is located in a different tectonic domain: European, IGB and Adriatic, respectively. Both the European and the Adriatic domains (Figs 4d and f) present a local velocity structure with a positive gradient from the surface down to *ca*. 12–16 km depth. We observe a slower crustal $v_S$ structure on the European side than on its Adriatic counterpart (Fig. 4f), extending from *ca*. 20 to 35 km depth (Fig. 4d). Both the European and the Adriatic profiles show a sharp velocity increase associated with the Moho discontinuity, where $v_S$ reaches 4 km s$^{-1}$, though at different depths: *ca*. 30 km depth on the Adriatic side (Fig. 4f) and *ca*. 50 km depth on the European side (Fig. 4d).

Strikingly different from the previous two zones, the structure associated with the IGB anomaly presents higher velocities at shallower depths (Fig. 4e): $v_S$ exceeds 3.6 km s$^{-1}$ at the surface and the shallowest crustal layer, and reaches more than 4 km s$^{-1}$ at *ca*. 25–30 km depths.

Horizontal slices through the model reveal that the velocity distribution correlates well in space with geological units mapped at the surface and the main tectonic structures in the same area, and points at some new features (Fig. 5). At depths from 2 to 10 km we identify the dominant contribution of the slow Po plain sediments, which is clearly visible to the southeast of the PL (Figs 5a–c), in contrast with the fast crustal structure on the northwestern side of the Insubric segment of the PL (Figs 5a–c).

Most importantly, we image a shallow and isolated high-velocity anomaly, prominently visible on the 2 and 5 km depth sections of the model at the centre of the study area (Figs 5a and b). The location of this shallow high-velocity anomaly corresponds well with the location of the IVZ lower-to-middle crustal and mantle peridotite outcrops exposed at the surface (Fig. 1). This high-velocity feature, located in correspondence of the two westernmost stations of the IvreaArray profile, and which we associate with the shallow-lying IGB in the IVZ (see discussion in Section 6), becomes elongated and continuous along the PL at 10 km depth (Fig. 5c). This highlights that the velocity structure varies both with depth, and along the main tectonic boundary. At increasing depths from 2 to 10 km below the surface, the high-velocity IGB anomaly evolves from local in the IVZ (Fig. 5a) to elongated along the strike of the European–Adriatic collision (Fig. 5c). Deeper in the crust, the European side shows velocities slower than in Adria; however, this slower trend is located further to the north-west with respect to PL (Figs 5e and f).

To image the structure of the continental collision at depth and its variation along strike, we analyse velocity variations along

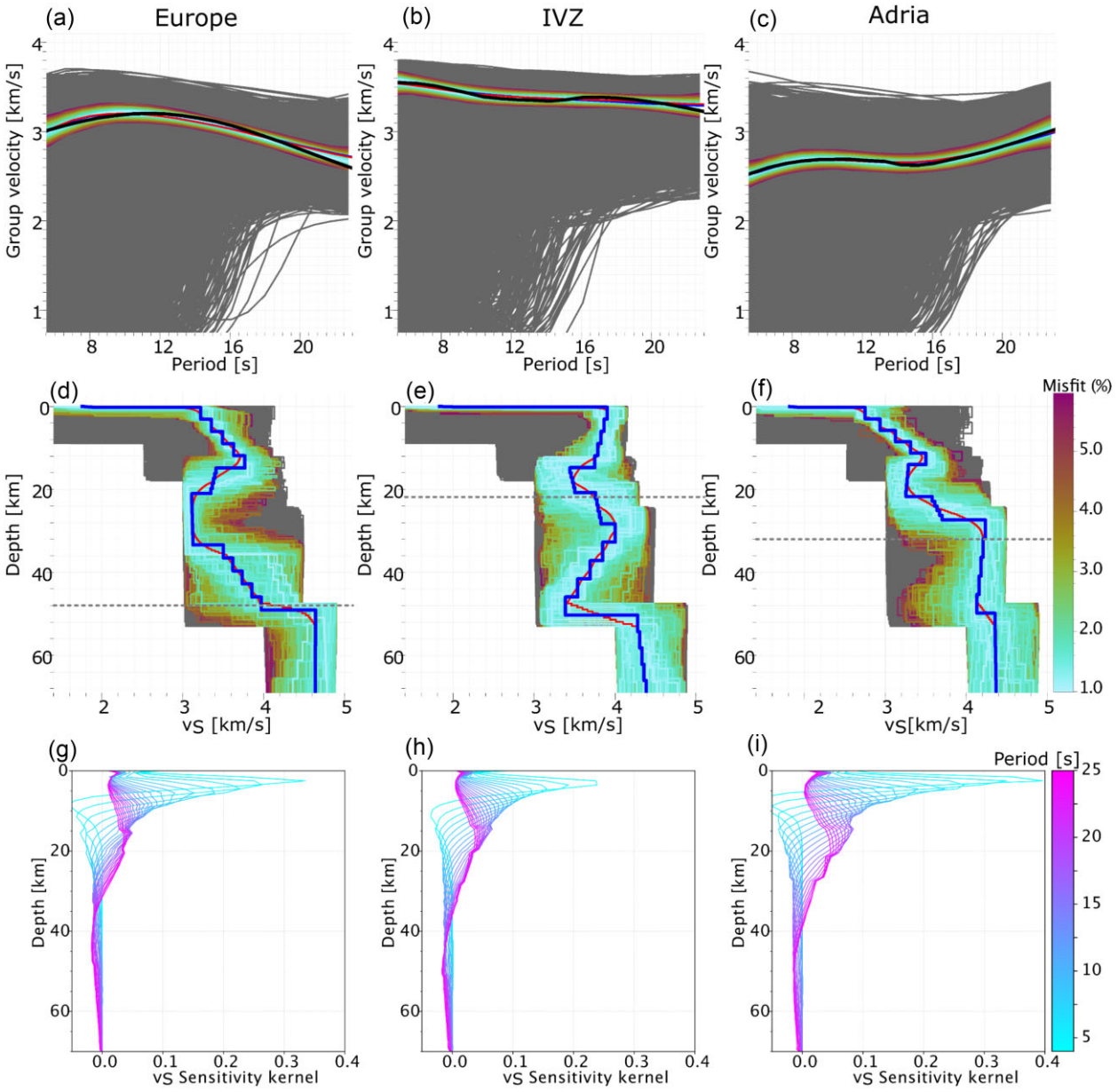


**Figure 4.** Examples of modelled dispersion curves at three different locations along the IvreaArray profile: Europe, IVZ, Adria (marked as locations *a*, *b* and *c* respectively in Fig. 3(a). (a)–(c) The observed (black) dispersion curves are compared with synthetic ones: the layer-averaged (blue) and depth-averaged (red) models, respectively. Both layer and depth averages are computed based on the best 10 per cent performing models (shown in colour); the remaining models are shown in grey. (d)–(f) The corresponding 1-D $v_S$ velocity models obtained from the inversion with the improved stochastic NA (Wathelet 2008): the layer-averaged (blue, used for the final 3-D model) and depth-averaged (red) models. The best 10 per cent models are shown in colour, the remaining ones in grey. The local Moho depth from Spada *et al.* (2013) is shown for reference (grey dashed line). (g)–(i) Group-velocity sensitivity kernels for the fundamental mode of Rayleigh waves for $v_S$ from period 4 s (cyan) to 25 s (magenta).

several vertical cross-sections through the model (Fig. 6). A pronounced and shallow high-velocity anomaly is observed beneath the IVZ along profile P2, which corresponds to the IGB (Fig. 6a), and reaches the surface at the location of the lower crustal and Balmuccia mantle-peridotite outcrops. High-velocity features at upper crustal levels are also visible along profiles P1 and P3, crossing the southern and the northern parts of the IVZ, respectively (Figs 6b and c), though without reaching the surface as in profile P2, but culminating rather at 10–15 km depth, respectively. Despite the overall $v_S$ sensitivity decrease at *ca*. 30–35 km depth (Figs 4g–i), we identify a major velocity increase along all the profiles P1, P2 and P3, which correlates well with the previous Moho discontinuity mapped by Spada *et al.* (2013—Figs 6a–c), with a sharper and better matching gradient on the Adria side, in particular.

## 6 DISCUSSION

Performing ANT with the IvreaArray seismic data provides new results on the geometry and the physical properties of the shallow

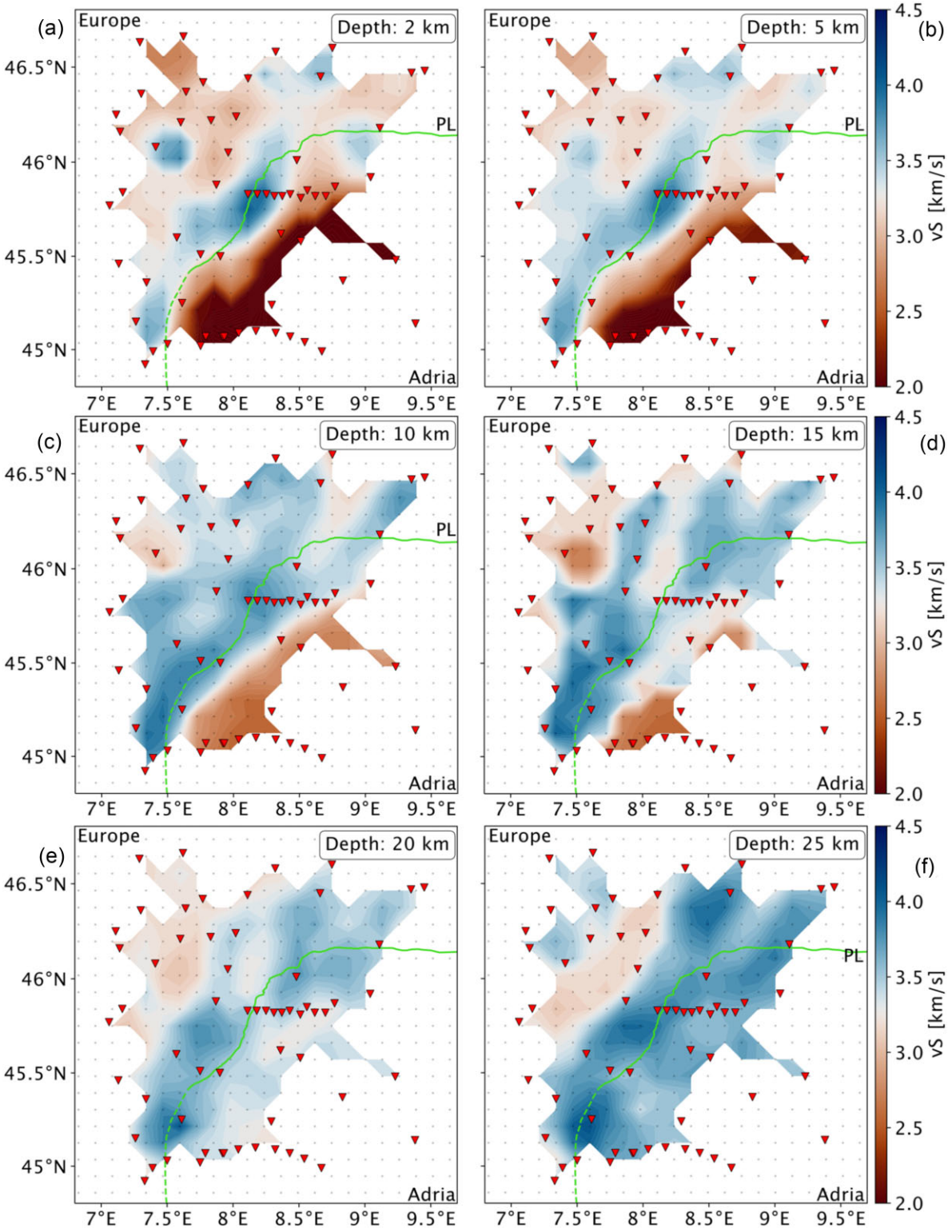


**Figure 5.** (a)–(f) Horizontal slices through the final 3-D $v_S$ model at different depths. The 1-D depth inversion was performed for each gridpoint, which counted at least at 10 rays, and the resulting 1-D models were combined to the final 3-D model shown in this figure. The PL and the seismic stations are shown for reference.

crust and of the IGB structure. These results can be interpreted in comparison with previous geophysical investigations in the same area, and the geological observations at the IVZ surface.

For this purpose, the east–west oriented IvreaArray profile represents a key transect, along which we can compare the present results directly with the recent RF and gravity studies (Scarponi *et al.* 2020, 2021). At the centre of this profile, our $v_S$ model clearly maps a distinct high-velocity anomaly at the Europe–Adria collision boundary (8.2° longitude), extending from the surface down to *ca*. 10–12 km depth. We interpret it as the fastest and shallowest portion of the

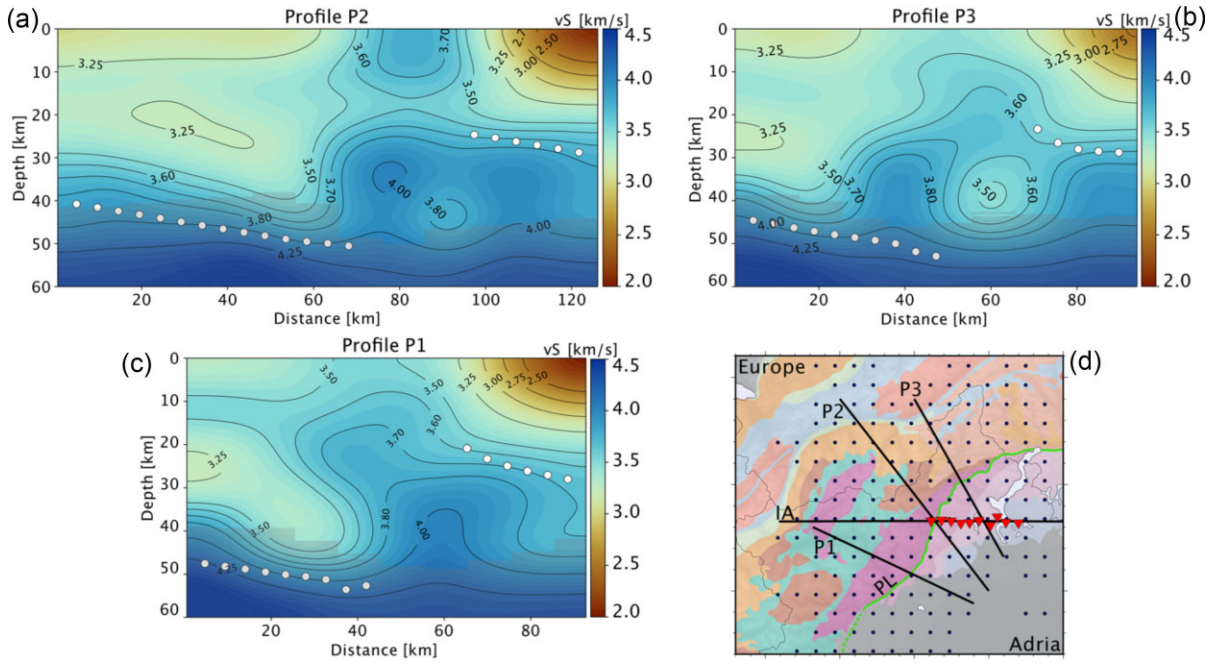


**Figure 6.** (a)–(c) Vertical cross-sections of the 3-D $v_S$ model along three profiles P1, P2 and P3. The white dots show an interpolation of the Moho map from Spada *et al.* (2013) along the considered profiles. Grey-shaded areas indicate parts of the model, where the sensitivity kernels have amplitudes lower than 5 per cent of their maximum, across all the periods of interest. (d) The location of the three profiles (P1, P2 and P3), together with the IvreaArray seismic stations and the map from Fig. 1 for reference. The profile IA is shown in Fig. 7. The black dots are the gridpoints where the NA inversion for the 1-D $v_S$ velocity profiles was performed.

IGB, reaching the surface within our resolution capabilities, and presenting $v_S$ values up to 3.8 km s$^{-1}$ at subsurface—up to 0 km to few km depths (Figs 7a).

To our knowledge, this is the first evidence of a shallow-lying IGB beneath the IVZ mantle and lower crustal outcrops, from $v_S$ tomography.

The resolved high $v_S$ anomaly correlates well with the shallowest portion of the 3-D IGB density model along the same profile (Fig. 7a), the latter obtained by previous independent gravity anomaly modelling (Scarponi *et al.* 2020).

The ANT results also agree with the independent 2-D RF migration analysis based on *P*-to-*S* conversions (Scarponi *et al.* 2021; Fig. 7b). The RF migration image shown in Fig. 7(b) should be interpreted as follows: positive (green) amplitudes represent an increase of seismic velocity with increasing depth, while negative (blue) amplitudes a decrease. RFs are useful in mapping the sharp contours of bulk velocity anomalies. In this case, the RF migration image shows a sharp increase in seismic velocity at the top of the IGB, which corresponds well with the shallow high-velocity anomaly mapped by ANT (red boxes, Fig. 7b). A good agreement is also observed on the Adriatic side further to the east, in correspondence of the Moho-related positive velocity gradient (red boxes, Fig. 7b).

However, such shallow, sharp velocity discontinuities can produce multiple reflections, which may mask later signals in the RFs, making deeper features less reliable for interpretation (pink and white boxes, Fig. 7b). This could be the case for the negative RF signal mapped in correspondence of an ANT low-velocity feature at *ca*. 40 km depth (white box, Fig. 7b), which presents good agreement in terms of location among the two methods. This slower feature is also visible further to the north along profile P3, and partially along profile P2 (Figs 6a and b). Along the IvreaArray profile, this is mapped only on one model gridpoint by ANT, and we do not regard it as well resolved. If real, it could point towards $v_S$ heterogeneities within the IGB at lower crustal depths, and warrants attention in future local investigations.

Our new results are also consistent with the best-performing model geometries from the 2-D joint RF and gravity inversion. There, the shallowest geometries reach 3–7 km depths in correspondence with the high-velocity feature resolved by ANT in this work (Fig. 7c, Scarponi *et al.* 2021). The agreement between the results of these two independent methods continues down to 30–40 km depths, where the modelled vertical structure bounds the high-velocity IGB in the crust.

In terms of large-scale structures, we observe consistent results in the European and Adriatic tectonic domains, with respect to the Moho mapped by Spada *et al.* (2013—Fig. 7a), the latter presenting a gap where we resolve the shallowest IGB portion at higher resolution. At the centre of the IVZ and perpendicular to the strike of the collision, the velocity contrast between the European and the IGB domains appears to be sharp throughout the whole crust (Fig. 6a), with systematically higher velocities on the Ivrea side (Figs 6a–c). A lower velocity structure west of the Ivrea body was also observed by Solarino *et al.* (1997) along the NW-SE ECORS-CROP transect further to south, and interpreted as the suture zone between the European and the Adriatic plates (Schmid & Kissling 2000).In our model, a slower European lower crust is visible throughout the whole study area, juxtaposed to the IGB high-velocity anomaly (Figs 6a–c).

We compare our model with the local earthquake tomography (LET) by Diehl *et al.* (2009). The LET approach results in a 3-D *P*-wave velocity model for the lithosphere, by simultaneously inverting for the hypocentres of local earthquakes and the surrounding 3-D velocity structure. In the case of Diehl *et al.* (2009), a new 3-D $v_P$ model is derived. We refer to their work for further details

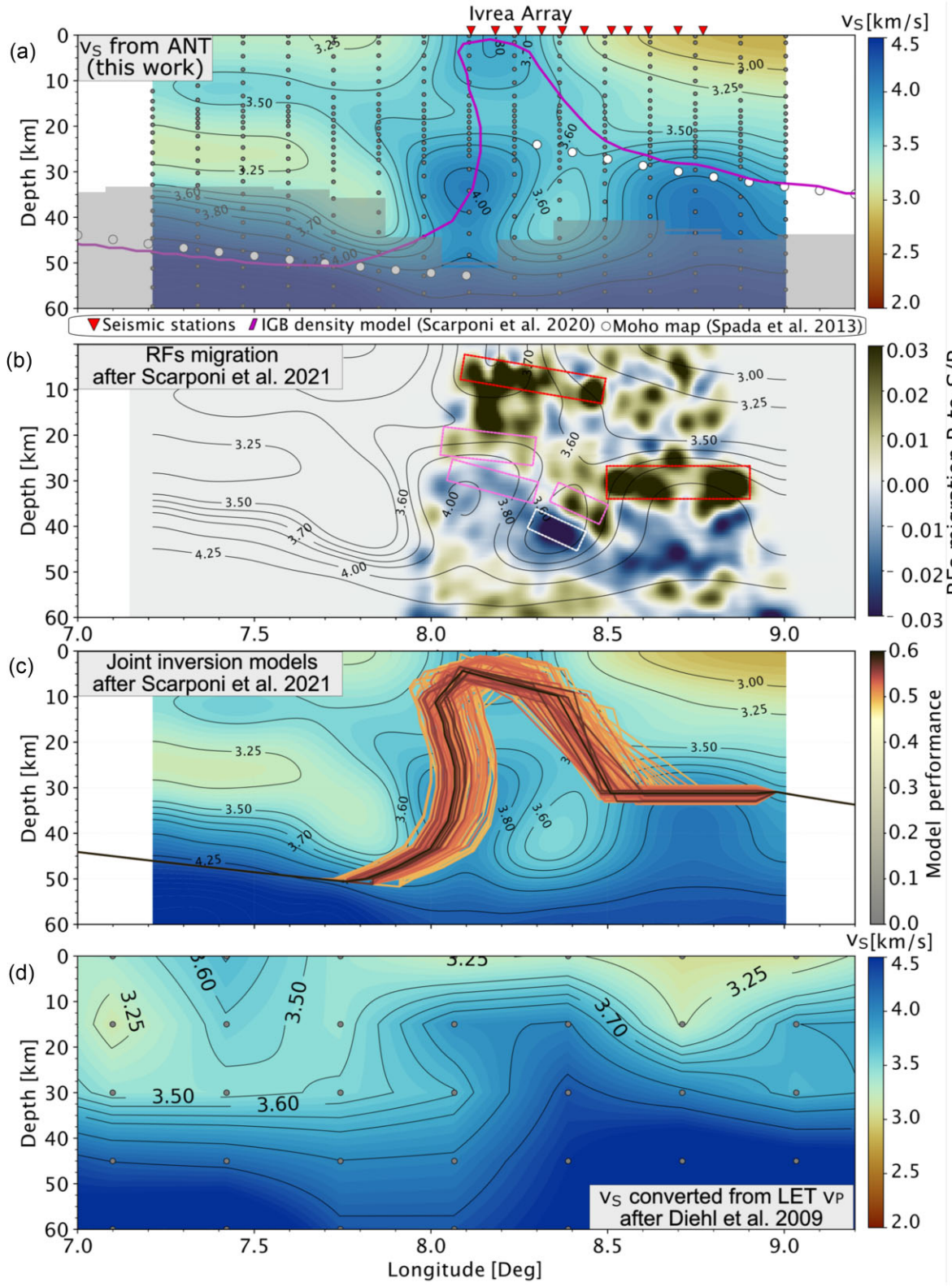


**Figure 7.** Comparison of various geophysical investigations and models along the west–east IvreaArray 'IA' profile (location in Fig. 6d). (a) Vertical cross-section of the 3-D $v_S$ model obtained in this study. White dots represent Moho depth from Spada *et al.* (2013), red triangles on top indicate the location of the IvreaArray seismic stations. Magenta contour represents the main density jump in cross-section of the 3-D IGB density model from gravimetry by Scarponi *et al.* (2020). Grey dots indicate the model nodes used in the NA inversion for the 1-D $v_S$ profiles. In the grey-shaded areas, sensitivity kernels have amplitudes lower than 5 per cent of their maximum, across all the periods of interest. (b) *P*-to-*S* converted RF migration image for the best-performing model in the joint RF-gravity inversion of Scarponi *et al.* (2021), along the same profile. Green and blue colours respectively indicate increase and decrease of $v_S$ with depth. The $v_S$ contours obtained in this study are overlaid. (c) 150 best model geometries from the joint RF-gravity inversion of Scarponi *et al.* (2021): the darker the colour, the better fit to the data. (d) Model cross-section from LET by Diehl *et al.* (2009), converted to $v_S$ by using an average constant $v_P/v_S$ ratio of 1.73.

on the LET methodology. Eventually, for the sake of a qualitative comparison between the LET model and our final 3-D $v_S$ model, we converted the $v_P$ model from Diehl *et al.* (2009) to a $v_S$ model, by assuming a constant and average $v_P/v_S$ value of 1.73 for our study area (Solarino *et al.* 2018; Colavitti *et al.* 2022). Most importantly, the LET work by Diehl *et al.* (2009) locates high velocities representing the shallowest IGB portion only up to *ca*. 10–12 km depth, not suggesting any connection to the surface, similarly to what was obtained further to the south from the temporary passive seismic experiments CIFALPS I and CIFALPS II (Solarino *et al.* 2018; Paul *et al.* 2022). While the lack of IGB-to-surface connection may stem from the model and/or data resolution in the case of Diehl *et al.* (2009, given at 25 km horizontally and 15 km vertically) and CIFALPS II models, it could be a real feature in CIFALPS I (south of the IVZ), where no lower-to-middle crustal composition outcrops are exposed at the surface (e.g. Schmid *et al.* 2004; Paul *et al.* 2022). However, a final analysis of the IGB-surface connection along the latter profiles (CIFALPS I and II) requires locally higher resolution imaging.

Comparing with Diehl *et al.* (2009), we can also observe second-order structural differences in the seismically slower sediment area on the Adriatic side (most likely related to the Po plain area, Figs 7a and d) and also on the European side, where the Moho is generally deeper, and a relatively slower and deepening crustal structure is mapped by both methods.

Overall, and in comparison with previous tomographic works covering the same area (e.g. Diehl *et al.* 2009; Kästle *et al.* 2018; Lu *et al.* 2018; Solarino *et al.* 2018), we benefit from the additional coverage provided by the densely spaced IvreaArray stations' data (Fig. 2), which allowed us to image the shallow-lying connection between the IVZ lower-to-middle crustal rock outcrops and the IGB coming nearly abreast at an unprecedented resolution (Figs 7a and d).

While we also associate the high-velocity structure at *ca*. 30–40 km depth and 8.1° longitude with the IGB, the nature of the relatively lower velocity feature between 15 and 20 km depth and 8.2° longitude is less certain (Fig. 7a). Although it still presents a high velocity of 3.6 km s$^{-1}$ when compared to classical middle crustal depths, the 0.15 km s$^{-1}$ uncertainty on $v_S$ does not allow a firm conclusion.

The newly obtained constraints on the shallow IGB's physical properties can be also compared with the physical properties of the rock samples, which were collected across the IVZ outcrops and analysed in the laboratory by previous authors (e.g. Khazanehdari *et al.* 2000; Zappone & Kissling 2021). While these values come from two very different spatial scales (1-to-10 km vs 1-to-10 cm), their comparison can help to rule out and/or to discuss some candidate rocks for the composition of the subsurface physical structure. Based on this work, we suggest a 3.6–4.1 km s$^{-1}$ $v_S$ range (including uncertainties) for the IGB's shallow structure, beneath the IVZ outcrops (Fig. 7). In addition to this, previous 3-D and 2-D gravity modelling suggests a range of density values from *ca*. 2900 kg m$^{-3}$ to a maximum of 3200–3300 kg m$^{-3}$ for the same structure (Scarponi *et al.* 2020, 2021). These geophysical observations are compatible with the physical properties of some of the ultramafic rock samples collected in the IVZ and analysed in the laboratory, even though other ultramafic rock samples present higher $v_S$ and higher density values (Fig. 8). Ultramafic rocks, in particular mantle peridotites, were previously suggested as the possible main components for the IGB by Scarponi *et al.* (2020). While this hypothesis remains valid in light of the new geophysical results, the new $v_S$ constraints are also compatible with other lower crustal rock types, such as amphibolite, stronalite and gabbroic rocks (Fig. 8). Amphibolite gabbros were also suggested by Pistone *et al.* (2020) as the most likely IGB components, based on petrophysical modelling of larger scale $\rho$–$v_P$ geophysical observations. However, Pistone *et al.* (2020) had $v_P$ constraints available from larger scales LET by Diehl *et al.* (2009) and no high-resolution $v_S$ constraints (Lu *et al.* 2018; Kästle *et al.* 2018 provide much smoother models across the same area). It should also be noted that eclogite rocks may also contribute to the high-velocity anomaly associated with the IGB. Nevertheless, we do not suggest them as the main component of the IGB on the southern Alpine side of the continental collision, which should be rather dominated by high-temperature metamorphic rocks (Scarponi *et al.* 2020).

The comparison of rock properties across spatial scales should consider the effect of anisotropy, not only of the rock samples, but of passive geophysical methods, as for example RF samples mostly along vertically propagating rays, and ANT mostly along horizontally propagating signals.

Alder *et al.* (2021) and Kästle *et al.* (2022) have investigated azimuthal and radial $v_S$ anisotropy at larger spatial scales, and the patterns they observe are not clearly interpretable within our model area. In this regard, future analysis is needed (i.e. including Love waves) to highlight the possible characteristics of anisotropy at intracrustal scales in the IVZ.

At a much smaller scale, Khazanehdari *et al.* (2000) measured up to 5 per cent positive anisotropy ($v_{SV} > v_{SH}$) for the lower crustal and mantle rocks sampled at the IVZ surface, which may contribute with a bias up to 0.2 km s$^{-1}$ in our comparison between laboratory analysis and geophysical results (Fig. 8). Ultimately, the analysis of rock samples from the DIVE drilling project will provide new information on the anisotropic properties of the rock lithologies in the IVZ area (Pistone *et al.* 2017), and will allow an additional comparison with the current geophysical results.

Further structural discussion of our results is warranted in light of the recent high-resolution traveltime tomography, performed at km-scales across the Balmuccia mantle peridotite outcrop with new controlled-source seismic data (Ryberg *et al.* 2023). The $v_P$ model by Ryberg *et al.* (2023) presents a continuous fast structure extending and broadening from the surface mantle peridotite outcrop down to maximum 3 km depth below sea level; this, together with our findings, suggests that the Balmuccia outcrop is likely the exposed portion of a protuberant body, and not only a surficial lens embedded in lower crustal rocks as referred to by Quick *et al.* (2003). Our results support the shallow, km-scale interpretation of Ryberg *et al.* (2023) and the possible existence of a mantle rock body continuously extending from the surface, producing a high-velocity anomaly within the whole upper crust. Based on our new 3-D $v_S$ model, we corroborate the model for which the entire crust was tilted and brought up to the surface, without major internal deformation (e.g. Zingg *et al.* 1990).

This suggests that peridotites may contribute to the high-velocity anomaly we resolve in the IVZ. Hence, the IGB geophysical anomaly may consist of a combination of both mantle peridotite and lower crustal rocks, bound in a complex and heterogeneous structure, whose internal distribution lies at spatial scales below the resolution of ANT. Based on these, we provide a new structural interpretation of the IGB along a linear NW-SE reference profile, crossing the IVZ perpendicularly to the main strike of the Europe–Adria collision, and centred on the Balmuccia mantle peridotite outcrop (Fig. 9). The new $v_S$ model and the surface geological observations together enable association of the base of the IGB with Adriatic mantle rocks, and its shallower portion with a heterogeneous

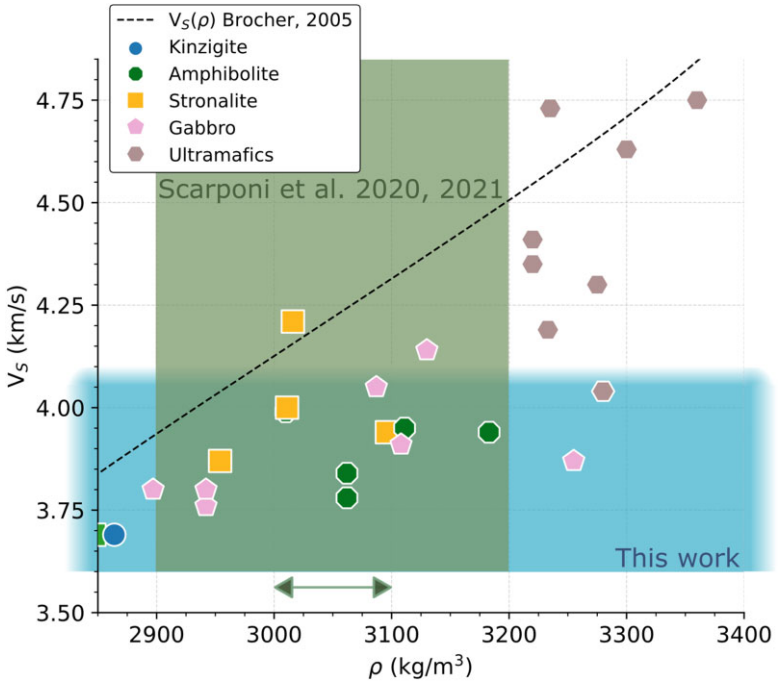


**Figure 8.** Comparing physical properties across scales, between the 1–10 cm size rock samples collected across the study area, and the constraints obtained from larger scale (>10 km) passive geophysical studies. The green area represents constraints on density and $v_S$, obtained from previous joint seismology-gravimetry inversion (Scarponi *et al.* 2020, 2021). The blue area represents constraints on $v_S$ only, as obtained from seismic ANT in this work. Both areas represent the physical properties of the shallow crustal geophysical anomaly associated with the IGB. As the gravity inversion constrains density contrasts and not absolute values, the green box can be rigidly translated along the *x*-axis by up to 100 kg m$^{-3}$. Finally, the scatter plot shows the rock physical property data from the SAPHYR catalogue (Zappone & Kissling 2021) for samples collected in the IVZ (Fig. 1). The black dashed line represents the $v_S$–$\rho$ (velocity–density) relationship obtained by regression on laboratory data (Brocher 2005).

structure, featuring lower crustal and mantle rocks at shallow depths beneath the IVZ. At greater depth, the base of the IGB penetrates further to the west and neighbours the European lower crust in place with the largest Moho offset between the European and the Adriatic Mohos. The shape of this structure generally follows that resolved by the 3-D gravity modelling and the 2-D joint gravity-RF inversion. The crustal structure from surface sediments to Moho, bent and tilted towards the surface during the continental tectonic collision, now displays subhorizontal (instead of vertical) layering at the IVZ surface. Further to west of the IVZ, at depth, the structures must have been affected by the emplacement of the IGB and the deformation along the PL, but remain unresolvable with passive geophysical methods.

As the nature and the characteristics of a palaeo-Moho transition zone beneath the IVZ still constitute open targets under investigation, the ongoing scientific drilling project DIVE may provide unprecedented information on physical properties across a range of scales (Pistone *et al.* 2017—http://www.dive2ivrea.org/). In particular, DIVE-phase II aims at performing a 4-km-deep drilling in the Balmuccia peridotite area, enabling a direct comparison with the current geophysical results in the near future and further advancing our understanding of the IGB and the continental lower crust.

## 7 CONCLUSIONS

We present a new 3-D shear wave seismic velocity model for the crust in the IVZ, derived from ANT, via an NA algorithm inversion of Rayleigh group-velocity dispersion curves (fundamental mode). We achieved higher resolution at crustal depths (i.e. minimum horizontal length-scale of 20 km) with respect to previous tomographic works targeting the Western Alps, by processing ambient noise data from both permanent and temporary seismic stations, in addition to the seismic data from the temporary IvreaArray network; the latter designed to locally investigate the IVZ subsurface.

The new detailed image of the IGB anomaly in the IVZ shows a unique structure and physical properties with respect to the neighbouring European and Adriatic domains. The physical structure associated with the IGB presents a shear wave seismic velocity of at least 3.6 km s$^{-1}$ directly from the surface, increasing up to 4 km s$^{-1}$ at 20–25 km depth. This shallow fast-velocity anomaly, within our resolution, reaches the surface in remarkable agreement with the location of the lower-to-middle crustal composition rocks and the Balmuccia peridotite exposed in the IVZ. This suggests a likely continuity between the surface geological observations and the subsurface geophysical anomalies.

Furthermore, the analysis of both vertical and horizontal cross-sections of the model indicates important variations in the IGB structure along the continental collision boundary. While the high-velocity IGB anomaly reaches its shallowest depth (surface) in the Balmuccia area, the related anomaly extends up to 10 and 15 km depth beneath the southern and northern edges of the IVZ respectively, similarly to the findings of other tomographic studies in the southwest of IvreaArray (CIFALPS I and CIFALPS II experiments, e.g. Solarino *et al.* 2018; Paul *et al.* 2022). The comparison with the results from both the joint and separate RFs and gravity-anomaly modelling (Scarponi *et al.* 2020, 2021) further supports the interpretation of a very shallow reaching (and possibly outcropping) IGB

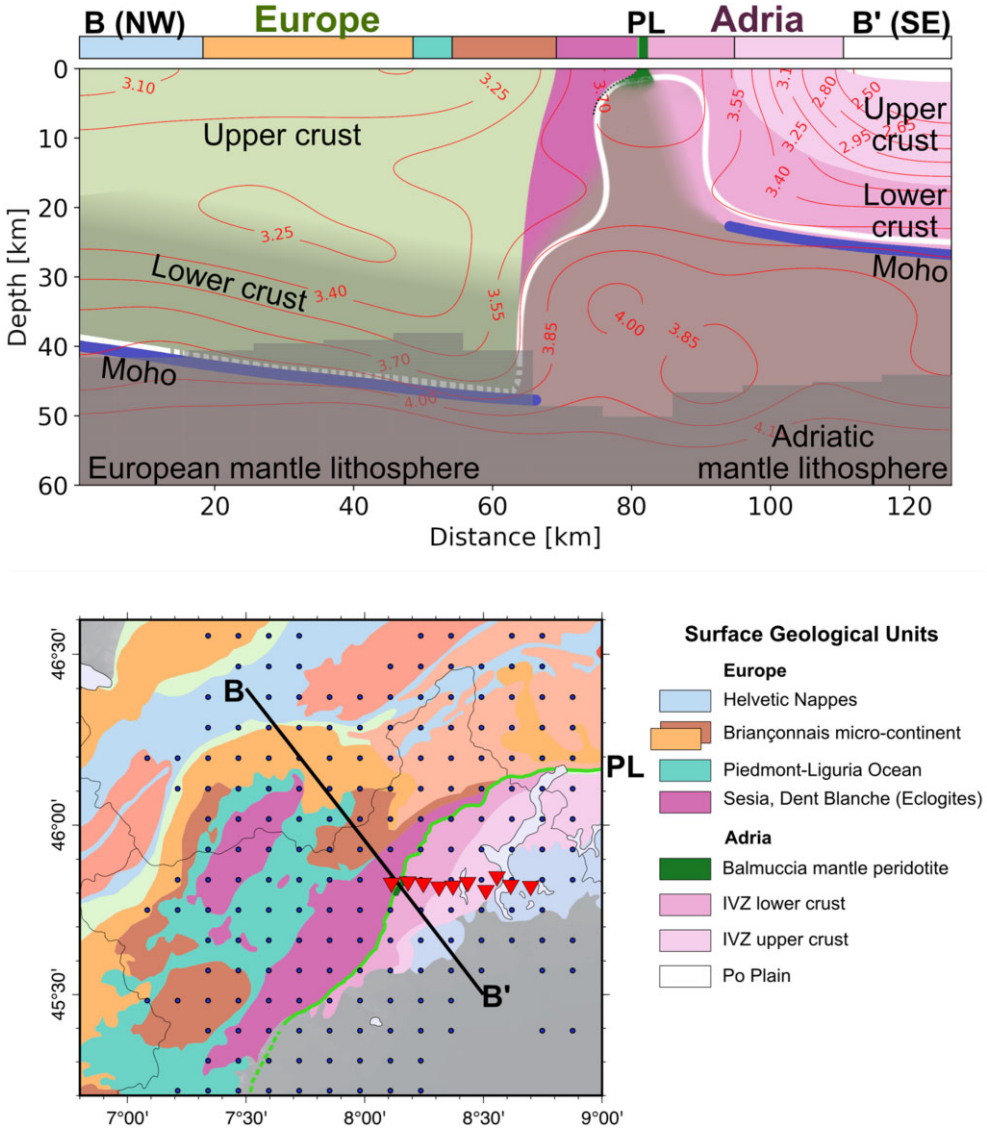


**Figure 9.** Geophysical interpretation of the $v_S$ model obtained in this study, along profile P2 crossing the PL. The top banner shows the tectonic units at the surface along the profile, as mapped in Figs 1 and 6(d) and in the inset below. The 'Surface Geological Units' legend provides the colour code. In the interpretation plot, red lines represent the $v_S$ iso-contours (in km s$^{-1}$) of the final model; blue lines identify the Moho on both the European and the Adriatic sides, traced after Spada *et al.* (2013); the white curve contours the physical structures associated with the IGB anomaly. Grey-shaded areas indicate parts of the model, where the sensitivity kernels have amplitudes lower than 5 per cent of their maximum, across all the periods of interest. We use green for European crust; white and pink for Adriatic sediments and crust; purple for eclogite rocks; green for mantle peridotite and brown for European and Adriatic mantle.

beneath the IVZ area. In addition to the IGB features, we also resolve second-order velocity variations in the neighbouring regions, featuring a slower European lower crust with respect to its Adriatic counterpart. We also resolve a deeper positive velocity increase, which agrees well, to the first order, with the Moho discontinuity previously mapped by Spada *et al.* (2013). Moreover, we resolve the faster IGB structure where the previous Moho map presented a gap.

We also observe agreement between the IGB velocities and the physical properties of the rock samples collected in the IVZ and analysed in the laboratory (Zappone & Kissling 2021). By also considering the density value ranges indicated by Scarponi *et al.* (2020, 2021), we argue that the bulk of the IGB may consist of a combination of mantle peridotite, ultramafic and lower crustal rocks. The current ANT model cannot resolve the signature of a potentially buried former Moho transition zone for the IVZ, which still constitutes a question of great interest and is worth future investigation with higher resolution approaches. Thanks to the dense IvreaArray seismic data, the new IGB model is more detailed and complex with respect to the iconic and long-time referred to as 'Bird's head' model by Berckhemer (1968).

Our new findings, based on new $v_S$ constraints in 3-D, corroborate the model of a continuous mantle-like body extending from the IVZ surface down through the whole crust, similarly to the recent interpretation of Ryberg *et al.* (2023) based on control source data $v_P$ tomography. This further suggests that the Balmuccia peridotite unit may not constitute an isolated lens, as previously hypothesized (e.g. Quick *et al.* 2003), and that the crustal cross-section exposed at the surface in the IVZ may have been tilted with minor internal deformation during the continental collision (e.g. Zingg *et al.* 1990). The direct analysis of new local rock samples expected from the outcome of the scientific drilling project DIVE may shed further

light on the IVZ subsurface composition at different scales, on the IGB structure and shape, as well as on the history of the upper-mantle to lower-crust material emplacement into the crust beneath the IVZ.

## SUPPORTING INFORMATION

Supplementary data are available at *GJI* online.

**Figure S0.** Topographic map of the study area, showing the seismic networks distribution and the PL (brown line) for reference.

**Figure S1.** Data availability diagram showing available seismic ambient noise recordings (in red) as a function of time, for all the considered stations in this study.

**Figure S2.** (a), (c), (e) and (g) Final ray paths are shown for the processed seismic ambient noise database, for selected periods at 6, 10, 18 and 23 s. (b), (d), (f) and (h) Azimuthal coverage across the study area. We analysed the retrieved ray paths (left-hand side of the figure) and computed azimuthal coverage at each point of the inversion grid, counting the ray azimuths in the intervals [0°, 45°], [45°, 90°], [90°, 135°], [135°, 180°], with angles defined clockwise from north. Gridpoints with azimuthal coverage of 4 (green cells on the map) count at least one ray in each of the azimuth intervals above.

**Figure S3.** Subset (*ca*. one-third of the total) of the ambient noise CC traces, computed and stacked via MSNoise software (Lecocq *et al.* 2014). After computation, the CC traces were filtered across different period ranges for the sake of display in (a)–(f). The 1–4 $km\,s^{-1}$ velocity range is shown (red dashed lines) in the causal and acausal sides of the traces. This same velocity range is then used for FTAN analysis picking.

**Figure S4.** 2-D Rayleigh group-velocity maps obtained from FMST, for selected periods.

**Figure S5.** A series of $v_S$ cross-sections along the west–east IvreaArray profile, as obtained from inversion tests, with increasing constraints on $v_S$ variation with depth. (a) No constraints on $v_S$ dependence with depth (setup adopted in the final inversion). (b) $v_S$ discontinuities are not allowed with depth. (c) $v_S$ is allowed ONLY to increase with depth. Setup (a) presents the minimum RMS. $v_S$ velocities in (a)–(c) are shown via iso-contours (black lines).

**Figure S6.** We show the distribution of the group envelope widths, as picked in the FTAN analysis, for selected periods of interest. Each peak histogram was approximated by a Gaussian distribution (black line); larger peaks (above $1\sigma$) were associated with a proportionally higher picking uncertainty in the subsequent FMST stage, for the computation of 2-D Rayleigh group-velocity maps.

**Figure S7.** Resolution tests at selected periods. The target distributions were obtained as realizations of a 2-D random Gaussian field with the addition of random noise; they are shown on the left-hand side of the figure in (a), (c), (e) and (g). On the right-hand side, the inversion results for the same selected periods in (b), (d), (f) and (h). RMS, smoothing and damping values are indicated for each test.

**Figure S8.** We show the summary of the test results, for the computation of the 2-D group-velocity maps at the period of 10 s. In particular, we show how the retrieved 2-D velocity models change as a function of the smoothing and damping parameters, in terms of: (a) traveltime RMS, (b) model roughness and (c) model variance. Red point locates our preferred choice for smoothing and damping parameters.

Please note: Oxford University Press is not responsible for the content or functionality of any supporting materials supplied by the authors. Any queries (other than missing material) should be directed to the corresponding author for the paper.

## ACKNOWLEDGMENTS

We thank the editor Gabi Laske, the reviewer Piero Poli and one anonymous reviewer for their constructive comments, which lead to an improved version of this manuscript. We would like to acknowledge many colleagues for their precious contributions and various inputs that made this work possible, both in the field and during the following steps; to P. Jedlička, J. Kotek and L. Vecsey from the Institute of Geophysics of the Czech Academy of Sciences, for the installation of the IvreaArray seismic stations (stations of MOBNET pool, granted by project CzechGeo/EPOS no. LM2015079 of the MEYS) and for the seismic data pre-processing, formatting and checking; to the members of the Lithosphere group of the Institute of Geophysics of the Czech Academy of Sciences L. Vecsey, H. Kampfová, H. Žlebčíková, C. Legendre and P Kolínský for the precious discussions and various inputs received during the development of this work; the whole IvreaArray working team for discussions and fieldwork efforts, together with numerous people in the field area for their help and support during the seismic sensor installation and maintenance: in particular to the mayors and the local contacts in the communes of Boccioleto, Vocca-Sassiglioni, Varallo, Civiasco, Cesara, Cheggino, Nebbiuno, Calogna, Ispra and Biandronno; to A. Zappone and T. Diehl for sharing background data and internal discussions. We are grateful for the support and the enthusiasm of many colleagues involved in the DIVE project, in particular Othmar Müntener, Alberto Zanetti, Mattia Pistone, Andrew Greenwood, Luca Ziberna and Klaus Holliger. We acknowledge the Swiss National Science Foundation (SNF) for having supported this research (grant nos PP00P2_157 627 and PP00P2_187 199 of project OROG3NY), as well as the Grant Agency of the Czech Republic (no. 21-25710S). We also acknowledge project CzechGeo/EPOS no. LM2015079 of the MEYS for funding the MOBNET station pool. MS and JP designed the study. MS and JK downloaded the data. MS performed the data processing and the inversion with guidance from JK and JP. MS and JP drafted the manuscript. MS, JK, GH, SS and JP discussed the obtained results. All authors revised the manuscript and approved the final version. No competing interests are associated with this research.

## DATA AVAILABILITY

All the seismic data used for this work is publicly open and accessible through the EIDA-ORFEUS (www.orfeus-eu.org) data centre under the FDSN network codes XK, IV, GU, MN, CH, YP and Z3. Any additional information for each seismic network at: XK, Hetényi *et al.* (2017); Z3, AlpArray Seismic Network (2018); IV, Istituto Nazionale di Geofisica e Vulcanologia (2005); MN, MedNet Project Partner Institutions (1990); CH, Swiss Seismological Service (SED) at ETH Zurich (1983); YP, Zhao *et al.* (2016); GU, University of Genova (1967).

## REFERENCES

Alder, C., Debayle, E., Bodin, T., Paul, A., Stehly, L. & Pedersen, H.& AlpArray Working Group, 2021. Evidence for radial anisotropy in the lower crust of the Apennines from Bayesian ambient noise tomography in Europe, *Geophys. J. Int.*, **226**(2), 941–967.

AlpArray Seismic Network, 2018. AlpArray seismic network (AASN) temporary component. *AlpArray Working Group.* doi: 10.1007/s10712-018-9472-4.

Ansorge, J., 1979. Crustal section across the zone of Ivrea-Verbano from the Valais to the Lago Maggiore.*BOLL. GEOFIS. TEOR. APPL,* **21,** 83, 149–157.

Bayer, R., Carozzo, M., Lanza, R., Miletto, M. & Rey, D.& Group, T. E.-C. G., 1989. Gravity modelling along the ECORS-CROP vertical seismic reflection profile through the Western Alps, *Tectonophysics,* **162**(3-4), 203–218.

Bensen, G., Ritzwoller, M., Barmin, M., Levshin, A.L., Lin, F., Moschetti, M., Shapiro, N. & Yang, Y., 2007. Processing seismic ambient noise data to obtain reliable broad-band surface wave dispersion measurements, *Geophys. J. Int.,* **169**(3), 1239–1260.

Berckhemer, H., 1968. Topographie des "Ivrea-Körpers" abgeleitet aus seismischen und gravimetrischen daten, *Schweiz. Mineral. Petrogr. Mitt,* **48**(1), 235–246.

Boschi, L., Weemstra, C., Verbeke, J., Ekström, G., Zunino, A. & Giardini, D., 2013. On measuring surface wave phase velocity from station–station cross-correlation of ambient signal, *Geophys. J. Int.,* **192**(1), 346–358.

Brocher, T.M., 2005. Empirical relations between elastic wavespeeds and density in the Earth's crust, *Bull. seism. Soc. Am.,* **95**(6), 2081–2092.

Bürki, B., 1990. *Geophysical Interpretation of Astrogravimetric Data in the Ivrea Zone, Exposed Cross-Sections of the Continental Crust,* Springer, pp. 545–561.

Closs, H. & Labrouste, Y., 1963. Recherches séismologiques dans les Alps Occidentales au moyen de grand explosions en 1956, *Mém. Coll. Année Géophys. Int.,* **XII-2**.Centre national de la recherche scientifiquepp. 241

Colavitti, L. & Hetényi, G.& AlpArray Working Group, 2022. A new approach to construct 3-D crustal shear-wave velocity models: method description and application to the Central Alps, *Acta Geod. Geophys.,* 1–34. doi: 10.1007/s40328-022-00394-4.

De Franco, R., Biella, G., Boniolo, G., Corsi, A., Demartin, M., Maistrello, M. & Morrone, A., 1997. Ivrea seismic array: a study of continental crust and upper mantle, *Geophys. J. Int.,* **128**(3), 723–736.

Diehl, T., Husen, S., Kissling, E. & Deichmann, N., 2009. High-resolution 3-DP-wave model of the Alpine crust, *Geophys. J. Int.,* **179**(2), 1133–1147.

Ekström, G., Abers, G.A. & Webb, S.C., 2009. Determination of surface-wave phase velocities across USArray from noise and Aki's spectral formulation, *Geophys. Res. Lett.,* **36**(18). doi: 10.5281/zenodo.1038209.

Fountain, D.M., 1976. The Ivrea—Verbano and Strona-Ceneri Zones, Northern Italy: a cross-section of the continental crust—new evidence from seismic velocities of rock samples, *Tectonophysics,* **33**(1-2), 145–165.

Handy, M.R., Schmid, S.M., Bousquet, R., Kissling, E. & Bernoulli, D., 2010. Reconciling plate-tectonic reconstructions of Alpine Tethys with the geological–geophysical record of spreading and subduction in the Alps, *Earth Sci. Rev.,* **102**(3-4), 121–158.

Handy, M.R., Ustaszewski, K. & Kissling, E., 2015. Reconstructing the Alps–Carpathians–Dinarides as a key to understanding switches in subduction polarity, slab gaps and surface motion, *Int. J. Earth Sci.,* **104**(1), 1–26.

Hetényi, G. *et al.* , 2017. IvreaArray—an AlpArray complementary experiment, Zenodo. doi: 10.5281/zenodo.1038209.

Hetényi, G. *et al.*, 2018. The AlpArray seismic network: a large-scale European experiment to image the Alpine orogen, *Surv. Geophys.,* **39**(5), 1009–1033.

Istituto Nazionale di Geofisica e Vulcanologia (INGV). Rete 2005 *Sismica Nazionale (RSN)*. Istituto Nazionale di Geofisica e Vulcanologia (INGV). doi: 10.13127/SD/X0FXNH7QFY.

Kästle, E.D., El-Sharkawy, A., Boschi, L., Meier, T., Rosenberg, C., Bellahsen, N., Cristiano, L. & Weidle, C., 2018. Surface wave tomography of the Alps using ambient-noise and earthquake phase velocity measurements, *J. geophys. Res.: Solid Earth,* **123**(2), 1770–1792.

Kästle, E.D., Molinari, I., Boschi, L. & Kissling, E.& AlpArray Working Group, 2022. Azimuthal anisotropy from eikonal tomography: example from ambient-noise measurements in the AlpArray network, *Geophys. J. Int.,* **229**(1), 151–170.

Khazanehdari, J., Rutter, E. & Brodie, K., 2000. High-pressure-high-temperature seismic velocity structure of the midcrustal and lower crustal rocks of the Ivrea-Verbano zone and Serie dei Laghi, NW Italy, *J. geophys. Res.: Solid Earth,* **105**(B6), 13843–13858.

Kissling, E., 1993. Deep structure of the Alps—what do we really know?, *Phys. Earth planet. Inter.,* **79**(1-2), 87–112.

Kissling, E., Schmid, S.M., Lippitsch, R., Ansorge, J. & Fügenschuh, B., 2006. Lithosphere structure and tectonic evolution of the Alpine arc: new evidence from high-resolution teleseismic tomography, *Geol. Soc. Lond. Mem.,* **32**(1), 129–145.

Kissling, E., Wagner, J. & Mueller, S., 1984. Three-dimensional gravity model of the northern Ivrea-Verbano Zone, Wagner, J.-J.& & Müller, St.(Eds.), *Geomagnetic and Gravimetric Studies of the Ivrea Zone*: Matér. Géol. Suisse. Géophys, vol. **21,** pp. 55–61.

Kvapil, J., Plomerová, J., Kampfová Exnerová, H., Babuška, V. & Hetényi, G.& Group, A. W., 2021. Transversely isotropic lower crust of variscan central Europe imaged by ambient noise tomography of the Bohemian Massif, *Solid Earth,* **12**(5), 1051–1074.

Lecocq, T., Caudron, C. & Brenguier, F., 2014. MSNoise, a python package for monitoring seismic velocity changes using ambient seismic noise, *Seismol. Res. Lett.,* **85**(3), 715–726.

Lehujeur, M., Vergne, J., Schmittbuhl, J., Zigone, D. & Le Chenadec, A.& EstOF Team, 2018. Reservoir imaging using ambient noise correlation from a dense seismic network. *J. geophys. Res.: Solid Earth,* **123**(8), 6671–6686.

Levshin, A. & Ritzwoller, M., 2001. *Automated Detection, Extraction, and Measurement of Regional Surface Waves, Monitoring the Comprehensive Nuclear-test-ban Treaty: Surface Waves,* Springer, pp. 1531–1545.

Lin, F.-C., Moschetti, M.P. & Ritzwoller, M.H., 2008. Surface wave tomography of the western United States from ambient seismic noise: Rayleigh and Love wave phase velocity maps, *Geophys. J. Int.,* **173**(1), 281–298.

Lippitsch, R., Kissling, E. & Ansorge, J., 2003. Upper mantle structure beneath the Alpine orogen from high-resolution teleseismic tomography, *J. geophys. Res.: Solid Earth,* **108**(B8). doi: 10.1029/2002JB002016.

Lobkis, O.I. & Weaver, R.L., 2001. On the emergence of the Green's function in the correlations of a diffuse field, *J. acoust. Soc. Am.,* **110**(6), 3011–3017.

Lu, Y., Stehly, L., Paul, A. & Group, A.W., 2018. High-resolution surface wave tomography of the European crust and uppermost mantle from ambient seismic noise, *Geophys. J. Int.,* **214**(2), 1136–1150.

MedNet Project Partner Institutions. 1990. *Mediterranean Very Broadband Seismographic Network (MedNet)*. Istituto Nazionale di Geofisica e Vulcanologia (INGV). doi: 10.13127/SD/fBBBtDtd6q.

Molinari, I., Argnani, A., Morelli, A. & Basini, P., 2015a. Development and testing of a 3D seismic velocity model of the Po Plain sedimentary basin, Italy, *Bull. seism. Soc. Am.,* **105**(2A), 753–764.

Molinari, I., Verbeke, J., Boschi, L., Kissling, E. & Morelli, A., 2015a. Italian and Alpine three-dimensional crustal structure imaged by ambient-noise surface-wave dispersion, *Geochem. Geophys. Geosyst.,* **16**(12), 4405–4421.

Mordret, A., Rivet, D., Landès, M. & Shapiro, N.M., 2015b. Three-dimensional shear velocity anisotropic model of Piton de la Fournaise Volcano (La Réunion Island) from ambient seismic noise, *J. geophys. Res. Solid Earth,* **120,** 406–427.

Niggli, E., 1947. Über den zusammenhang zwischen der positiven schwereanomalie am Südfuß der Westalpen und der Gesteinszone von Ivrea. doi: 10.5169/seals-160786.

Nishida, K., Montagner, JP. & Kawakatsu, H., 2009. Global surface wave tomography using seismic hum, *Science,* **326**(5949). doi: 10.1126/science.1176389.

Nouibat, A., Stehly, L., Paul, A., Schwartz, S., Bodin, T., Dumont, T., Rolland, Y. & Brossier, R., 2022. Lithospheric transdimensional ambient-noise tomography of W-Europe: implications for crustal-scale geometry of the W-Alps, *Geophys. J. Int.,* **229,** 862–879.

Paul, A. *et al.* 2022. Along-strike variations in the fossil subduction zone of the Western Alps revealed by the CIFALPS seismic experiments and their implications for exhumation of (ultra-) high-pressure rocks, *Earth planet. Sci. Lett.,* **598,** 117843. doi: 10.1016/j.epsl.2022.117843.

Paul, A., Cattaneo, M., Thouvenot, F., Spallarossa, D., Béthoux, N. & Fréchet, J., 2001. A three-dimensional crustal velocity model of the south-western Alps from local earthquake tomography, *J. geophys. Res.: Solid Earth,* **106**(B9), 19367–19389.

Pedersen, H.A., Mattern, F., Poli, P. & Stehly, L., 2023. Imaging with seismic noise: improving extraction of body wave phases from the deep Earth through selective stacking based on H/V ratios, *Geophys. J. Int.,* **232**(2), 1455–1467.

Petri, B., Duretz, T., Mohn, G., Schmalholz, S.M., Karner, G.D. & Müntener, O., 2019. Thinning mechanisms of heterogeneous continental lithosphere, *Earth planet. Sci. Lett.,* **512,** 147–162.

Pistone, M., Müntener, O., Ziberna, L., Hetényi, G. & Zanetti, A., 2017. Report on the ICDP workshop DIVE (Drilling the Ivrea–Verbano zonE). *Sci. Drill.,* **23,** 47–56.

Pistone, M., Ziberna, L., Hetényi, G., Scarponi, M., Zanetti, A. & Müntener, O., 2020. Joint geophysical-petrological modeling on the Ivrea geophysical body beneath Valsesia, Italy, *Constr. Continental Lower Crust: Geochem. Geophys. Geosyst.,* **21**(12), e2020GC009397. doi: 10.1029/2020GC009397.

Qorbani, E., Kolínský, P., Bianchi, I., Zigone, D. & Bokelmann, G., 2022. Upper crustal structure at the KTB drilling site from ambient noise tomography, *Geophys. J. Int.,* **231**(2), 982–995.

Quick, J.E., Sinigoi, S. & Mayer, A., 1995. Emplacement of mantle peridotite in the lower continental crust, Ivrea-Verbano zone, northwest Italy, *Geology,* **23,** 739–742.

Quick, J.E., Sinigoi, S., Snoke, A.W., Kalakay, T.J., Mayer, A. & Peressini, G., 2003. Geologic map of the southern Ivrea-Verbano Zone, northwestern Italy, *US Geol. Surv.* doi: 10.3133/i2776.

Rawlinson, N., 2005. *FMST: Fast Marching Surface Tomography Package–Instructions,* Research School of Earth Sciences, Australian National University, Canberra, vol. **29,** p. 47.

Rivalenti, G., Garuti, G. & Rossi, A., 1975. The origin of the Ivrea-Verbano basic formation (western Italian Alps): whole rock geochemistry, *Soc. Geol. Ital. Boll.,* **94,** 1149–1186.

Rivalenti, G., Garuti, G., Rossi, A., Siena, F. & Sinigoi, S., 1981. Existence of different peridotite types and of a layered igneous complex in the Ivrea Zone of the Western Alps, *J. Petrol.,* **22,** 127–153.

Ryberg, T., Haberland, C., Wawerzinek, B., Stiller, M., Bauer, K., Zanetti, A. & Krawczyk, C.M., 2023. 3D imaging of the Balmuccia peridotite body (Ivrea-Verbano zone, NW-Italy) using controlled source seismic data, *Geophys. J. Int.,* ggad182. doi: 10.1093/gji/ggad182.

Salimbeni, S., Agostinetti, N.P., Pondrelli, S. & Group, C.W., 2020. Insights into the origin and deformation style of the continental Moho: a case-study from the Western Alps (Italy). *J. geophys. Res.: Solid Earth,* e2020JB021319. doi: 10.1029/2020JB021319.

Sambridge, M., 1999. Geophysical inversion with a neighbourhood algorithm—I. Searching a parameter space, *Geophys. J. Int.,* **138**(2), 479–494.

Sambridge, M. & Mosegaard, K., 2002. Monte Carlo methods in geophysical inverse problems, *Rev. Geophys.,* **40**(3), 3–1.

Sánchez-Pastor, P. *et al.*, 2021. Imaging high-temperature geothermal reservoirs with ambient seismic noise tomography, a case study of the Hengill geothermal field, SW Iceland, *Geothermics,* **96,** 102207. doi: 10.1016/j.geothermics.2021.102207.

Scarponi, M., Hetényi, G., Berthet, T., Baron, L., Manzotti, P., Petri, B., Pistone, M. & Müntener, O., 2020. New gravity data and 3-D density model constraints on the Ivrea Geophysical Body (Western Alps). *Geophys. J. Int.,* **222**(3), 1977–1991.

Scarponi, M., Hetényi, G., Plomerová, J., Solarino, S., Baron, L. & Petri, B., 2021. Joint seismic and gravity data inversion to image intra-crustal structures: the Ivrea Geophysical Body along the Val Sesia profile (Piedmont, Italy). *Front. Earth Sci.,* **9**. doi: 10.3389/feart.2021.671412.

Schimmel, M., Stutzmann, E. & Gallart, J., 2011. Using instantaneous phase coherence for signal extraction from ambient noise data at a local to a global scale. *Geophys. J. Int.,* **184**(1), 494–506.

Schippkus, S., Zigone, D. & Bokelmann, G., 2020. Azimuthal anisotropy in the wider Vienna basin region: a proxy for the present-day stress field and deformation. *Geophys. J. Int.,* **220**(3), 2056–2067.

Schmid, S., Aebli, H., Heller, F. & Zingg, A., 1989. The role of the Periadriatic Line in the tectonic evolution of the Alps, *Geol. Soc. Lond. Spec. Publ.,* **45**(1), 153–171.

Schmid, S. & Kissling, E., 2000. The arc of the western Alps in the light of geophysical data on deep crustal structure, *Tectonics,* **19**(1), 62–85.

Schmid, S.M., Fügenschuh, B., Kissling, E. & Schuster, R., 2004. Tectonic map and overall architecture of the Alpine orogen, *Eclogae Geol. Helv.,* **97**(1), 93–117.

Schmid, S.M., Kissling, E., Diehl, T., van Hinsbergen, D.J. & Molli, G., 2017. Ivrea mantle wedge, arc of the Western Alps, and kinematic evolution of the Alps–Apennines orogenic system, *Swiss J. Geosci.,* **110**(2), 581–612.

Shapiro, N.M. & Campillo, M., 2004. Emergence of broadband Rayleigh waves from correlations of the ambient seismic noise, *Geophys. Res. Lett.,* **31**(7). doi: 10.1029/2004GL019491.

Solarino, S. *et al.*, 2018. Mantle wedge exhumation beneath the Dora-Maira (U) HP dome unravelled by local earthquake tomography (Western Alps). *Lithos,* **296,** 623–636.

Solarino, S., Kissling, E., Cattaneo, M. & Eva, C., 1997. Local earthquake tomography of the southern part of the Ivrea body, North-Western Italy, *Eclogae Geol. Helv.,* **90**(2), 357–364.

Spada, M., Bianchi, I., Kissling, E., Agostinetti, N.P. & Wiemer, S., 2013. Combining controlled-source seismology and receiver function information to derive 3-D Moho topography for Italy, *Geophys. J. Int.,* **194**(2), 1050–1068.

Stehly, L., Campillo, M. & Shapiro, N., 2006. A study of the seismic noise from its long-range correlation properties, *J. geophys. Res.: Solid Earth,* **111**(B10). doi: 10.1029/2005JB004237.

Swiss Seismological Service (SED) at ETH Zurich, 1983. *National Seismic Networks of Switzerland,* ETH Zürich.

Thouvenot, F., Paul, A., Senechal, G., Hirn, A. & Nicolich, R., 1990. ECORS-CROP wide-angle reflection seismics: constraints on deep interfaces beneath the Alps, *Mém. Soc. Géol. France,* **156,** 97–106.

University of Genova, 1967. Regional Seismic Network of North Western Italy. International Federation of Digital Seismograph Networks. Other/Seismic Network. doi: 10.7914/SN/GU.

Verbeke, J., Boschi, L., Stehly, L., Kissling, E. & Michelini, A., 2012. High-resolution Rayleigh-wave velocity maps of central Europe from a dense ambient-noise data set, *Geophys. J. Int.,* **188**(3), 1173–1187.

Wathelet, M., 2008. An improved neighborhood algorithm: parameter conditions and dynamic scaling, *Geophys. Res. Lett.,* **35**(9). doi: 10.1029/2008GL033256.

Yang, Y. & Ritzwoller, M.H., 2008. Characteristics of ambient seismic noise as a source for surface wave tomography, *Geochem. Geophys. Geosyst.,* **9**(2). doi: 10.1029/2007GC001814.

Zappone, A. & Kissling, E., 2021. SAPHYR: Swiss Atlas of Physical Properties of Rocks: the continental crust in a database, *Swiss J. Geosci.,* **114**(1), 1–27.

Zhao, L. *et al.*, 2015. First seismic evidence for continental subduction beneath the Western Alps, *Geology,* **43**(9), 815–818.

Zhao, L. *et al.*, 2020. Evidence for a serpentinized plate interface favouring continental subduction, *Nat. Commun.,* **11**(1), 1–8.

Zhao, L., Paul, A. & Solarino, S.& RESIF, 2016. Seismic network YP: CIFALPS temporary experiment (China-Italy-France Alps seismic transect). RESIF (Réseau Sismologique et Géodésique Français). doi: 10.15778/RESIF.XT2018.

Zingg, A., Handy, M.R., Hunziker, J.C. & Schmid, S.M., 1990. Tectonometamorphic history of the Ivrea Zone and its relationship to the crustal evolution of the Southern Alps, *Tectonophysics,* **182**(1-2), 169–192.